AIMS Mathematics

https://www.aimspress.com/journal/Math

AIMS Mathematics, 11(8): 27529–27562.
DOI:10.3934/math.20261102
Received: 22 May 2026
Revised: 29 June 2026
Accepted: 08 July 2026
Published: 31 August 2026

Research article

A well-balanced and positivity-preserving central scheme for shallow water equations

Elissa Malaeb[1,*], **Toni Sayah**[1] **and Rony Touma**[2]

[1] Laboratoire de Mathématiques et Applications, Unité de recherche Mathématiques et Modélisation, CAR, Faculté des Sciences, Université Saint-Joseph de Beyrouth, B.P. 11-514 Riad El Solh, Beirut 1107 2050, Lebanon

[2] Department of Computer Science and Mathematics, Lebanese American University, Byblos, Lebanon

* **Correspondence:** Email: elissa.malaeb@net.usj.edu.lb.

Abstract: We present a robust central scheme for shallow water equations with wetting and drying that is formally second-order accurate in smooth regions. The proposed method preserves physically admissible states, particularly the non-negativity of the water height, while accurately resolving complex flows in the presence of dry areas without relying on Riemann solvers. The scheme combines a well-balanced discretization, the surface gradient formulation, with a nonlinear invariant-region-preserving limiter to ensure consistency between flux and source term discretizations, suppress spurious oscillations near wet–dry interfaces, and maintain the well-balanced property for steady states, including lake-at-rest configurations over irregular topographies. In dry and near wet–dry regions, the limiter preserves positivity, while in fully wet regions, it remains inactive so that the scheme locally recovers the original well-balanced formulation. A cutoff criterion is introduced to activate the limiter only when necessary, thereby preserving accuracy in fully wet regions. The main contribution of this work lies in the compatible coupling of the surface gradient reconstruction and invariant-region-preserving limiting within an unstaggered central framework, together with a dedicated treatment of lake-at-rest configurations involving wet–dry interfaces. Numerical experiments demonstrate second-order numerical convergence for the water height in smooth benchmark problems, as well as robustness and favorable performance compared with existing methods.

Keywords: Well-balanced central schemes; positivity-preserving reconstructions; shallow water equations; finite volume methods
Mathematics Subject Classification: 65M08

1. Introduction

Shallow water equations (SWE) constitute a fundamental model for free-surface flows arising in coastal and hydraulic engineering, river and flood dynamics, environmental flows, and geophysical applications. In realistic configurations, such flows are often governed by variable bottom topographies and may involve transitions between wet and dry regions. These features introduce several numerical difficulties, since a reliable discretization must preserve physically admissible states, maintain the non-negativity of the water height, and accurately capture steady-state solutions such as the lake-at-rest equilibrium. In particular, the interaction between wetting and drying mechanisms and steady-state preservation remains one of the major challenges in the numerical approximation of SWE.

Finite volume methods have been widely used for the numerical solution of SWE due to their conservative structure and robustness in the presence of nonsmooth solutions. Among them, central and central upwind schemes constitute attractive alternatives to classical upwind methods since they avoid, either completely or partially, the solution of Riemann problems at the cell interfaces. The pioneering work of Nessyahu and Tadmor introduced high-resolution staggered central schemes based on Monotonic Upstream-centered Scheme for Conservation Laws (MUSCL)-type reconstructions [1]. Later, Jiang et al. [2] proposed nonstaggered central schemes that retain the simplicity of central discretizations while evolving the numerical solution on a single grid, thereby simplifying the treatment of complex geometries and boundary conditions. These approaches rely on a careful discretization of the flux and source terms in order to preserve steady states at the discrete level. In particular, surface gradient methods (SGM) reconstruct the water height through the water surface elevation rather than directly, allowing the numerical scheme to preserve lake-at-rest equilibria with high accuracy [3]. Related central and central upwind approaches for hyperbolic systems and shallow water equations have also been extensively investigated [4–6], while central schemes for nonconservative hyperbolic systems have been studied in [7].

Another major difficulty in shallow water simulations concerns the preservation of positivity near wet–dry interfaces. Standard reconstructions may generate nonphysical negative water depths, especially in the presence of complex bottom topographies or nearly dry regions. To address this issue, several positivity-preserving and wet–dry well-balanced schemes have been developed, including finite-volume and central upwind approaches [8, 9], Weighted Essentially Non-Oscillatory (WENO) schemes [10], discontinuous Galerkin methods [11], and active flux methods [12]. In particular, central and unstaggered central schemes capable of handling wetting and drying while preserving positivity have been proposed in [13, 14], while invariant-region-preserving (IRP) reconstructions were incorporated into unstaggered central schemes in [15]. Additional well-balanced and positivity-preserving approaches have been developed for shallow water models with friction [16], while related methods addressing moving equilibria and complex flooding configurations have been investigated in [17–19]. Other numerical and analytical approaches for shallow water-type systems include predictor–corrector and fractional-step formulations as well as analytical solitary-wave models [20,21].

Beyond finite volume and central discretizations, finite element approaches have also been widely investigated for shallow water-type systems, particularly in multidimensional settings and on unstructured meshes where geometric flexibility becomes essential. Examples include finite element formulations on triangular meshes for shallow water models [22, 23]. More recently, enriched nonconforming finite element constructions based on Crouzeix–Raviart elements have been developed to improve approximation accuracy and computational efficiency [24, 25]. Such approaches provide promising directions for future extensions of shallow water discretizations to more general geometries and higher-dimensional settings.

Despite the significant progress achieved by existing well-balanced and positivity-preserving methods, the simultaneous treatment of wet–dry interfaces and steady-state preservation remains delicate within unstaggered central frameworks. In particular, enforcing positivity through nonlinear limiting procedures may interfere with the discrete balance between the flux gradients and source terms responsible for preserving lake-at-rest equilibria. This interaction becomes especially sensitive near wet–dry fronts, where limiter activation may occur even in equilibrium configurations and introduce artificial perturbations of the steady state. The difficulty is particularly pronounced for lake-at-rest configurations containing dry regions, where standard well-balanced and positivity-preserving mechanisms alone are insufficient to preserve the discrete equilibrium at the wet–dry interface.

The objective of this work is to develop a well-balanced positivity-preserving unstaggered central scheme for SWE with wetting and drying over smooth or discontinuous bottom topographies. The proposed method is based on a specific formulation of the well-balanced unstaggered central framework, in which a compatible coupling between the sensor-based SGM reconstruction and an IRP limiter is constructed so as to preserve the equilibrium structure of the scheme. This construction ensures positivity in dry and near wet–dry regions while preserving the original well-balanced formulation whenever limiter activation is unnecessary.

An important feature of the proposed method is the precise characterization of when limiter activation is required. In particular, Lemma 1 establishes explicit cutoff criteria preventing unnecessary limiter activation in fully wet regions, allowing the scheme to locally recover the original well-balanced discretization and preserve stationary states up to machine precision. The main novelty of this work lies in the treatment of lake-at-rest configurations involving wet–dry interfaces, where the standard combination of well-balancing and positivity preservation is no longer sufficient. To address this challenge, we introduce a dedicated wet–dry reconstruction for preserving lake-at-rest states together with a local balance law discretization over the wet portion of the dual cell. We also establish the well-balancedness of the proposed scheme through a rigorous proof of the C-property. The resulting method provides a second-order central scheme without Riemann solvers.

The main contributions of this work can be summarized as follows. First, we develop a compatible coupling between the sensor-based SGM and the IRP limiter within an unstaggered central finite-volume framework, ensuring that positivity preservation does not compromise the well-balanced property. Second, we derive a cutoff criterion that prevents unnecessary limiter activation in fully wet regions, allowing the method to recover the original well-balanced discretization whenever positivity is not at risk. Third, we introduce a dedicated wet–dry reconstruction together with a local source-term discretization for discrete lake-at-rest configurations involving wet–dry interfaces, leading to exact preservation of the equilibrium states and dry regions. Finally, we provide a theoretical analysis of the proposed methodology together with extensive one-dimensional numerical experiments that demonstrate its robustness, well-balanced behavior, positivity preservation, and favorable performance compared with existing methods.

This treatment preserves the C-property at wet–dry interfaces while maintaining non-negative water heights under the proposed positivity-preserving reconstruction and the corresponding Courant–Friedrichs–Lewy (CFL) restriction. Numerical experiments provide extensive validation of the proposed approach and demonstrate second-order numerical convergence for water height in smooth benchmark problems, together with robustness for challenging wet–dry configurations involving discontinuous topographies and dam-break-type flows.

The remainder of the paper is organized as follows. Section 2 presents the numerical scheme and the proposed wet–dry treatment. Sections 3 and 4 report the numerical experiments in one and two dimensions, respectively.

2. Governing equations and numerical scheme

In this section, we consider the one-dimensional nonhomogeneous shallow water system and recall the classical well-balanced unstaggered central scheme [4], originally designed for fully wet domains. In Subsection 2.1, we extend this formulation to allow for wet–dry transitions through the introduction of a nonlinear limiting procedure, namely the IRP limiter [15], defined in (2.16). This extended scheme is capable of handling general wet–dry configurations as well as lake-at-rest states in fully wet regions. However, it does not guarantee the preservation of the lake-at-rest equilibrium in the presence of wet–dry interfaces. This limitation is addressed in Subsection 2.2, where we introduce a dedicated treatment that restores both the well-balancedness and positivity, leading to the proposed numerical scheme.

The one-dimensional shallow water system over a nonuniform bottom, expressed in conservative balance-law, reads as follows:

$$\begin{cases} \partial_t \mathbf{u} + \partial_x f(\mathbf{u}) = S(\mathbf{u}, x), \quad t > 0,\ x \in \Omega \subset \mathbb{R}, \\ \mathbf{u}(x, 0) = \mathbf{u}_0(x), \end{cases} \tag{2.1}$$

where the conservative state vector, flux function, and source term are defined by

$$\mathbf{u} = \begin{pmatrix} h \\ hu \end{pmatrix}, \qquad f(\mathbf{u}) = \begin{pmatrix} hu \\ hu^2 + \dfrac{1}{2} g h^2 \end{pmatrix}, \qquad S(\mathbf{u}, x) = \begin{pmatrix} 0 \\ -gh\, b_x \end{pmatrix}. \tag{2.2}$$

In this formulation, $h(x, t)$ represents the water depth, $u(x, t)$ denotes the scalar flow velocity, g is the gravitational constant, and $b(x)$ is the prescribed bottom profile. Throughout this manuscript, the boldface notation $\mathbf{u}$ is used exclusively to denote the conservative state vector, whereas the nonbold symbol u refers only to the scalar velocity variable.

A fundamental requirement for any reliable numerical method applied to (2.1) is the accurate preservation of steady-state solutions. In this context, well-balanced methods aim to preserve the equilibria of the shallow water system, including both the classical lake-at-rest configuration and more general steady states such as moving water equilibria with a nonzero velocity or steady flows over variable bottom topography. Among these, the lake-at-rest configuration

$$h + b = \text{const}, \qquad u = 0,$$

commonly referred to as the C-property, plays a central role. Satisfying this property at the discrete level is crucial for preventing nonphysical oscillations and for maintaining equilibrium states.

The numerical scheme presented in this section combines several established ingredients, namely the unstaggered central framework, the sensor-based surface gradient reconstruction, and IRP limiting strategies. These components are not new individually and are adopted from earlier works.

The novelty of the present method lies in their specific integration within a unified well-balanced positivity-preserving framework for shallow water flows with wetting and drying. In particular, Lemma 1 characterizes when the limiter remains inactive so that the original well-balanced discretization is recovered in fully wet regions. The main new component is the treatment developed in Subsection 2.2 for discrete lake-at-rest configurations involving wet–dry interfaces.

2.1. Numerical scheme with a nonlinear limiter

We consider the computational domain Ω as an interval of the real line, which is discretized into a set of control cells defined by $C_i = [x_{i-1/2}, x_{i+1/2}]$. The computational domain is partitioned into cells $C_i = [x_{i-1/2}, x_{i+1/2}]$ of a constant size $\Delta x = x_{i+1/2} - x_{i-1/2}$, with the cell centers located at x_i. We also define the dual cells $D_{i+1/2} = [x_i, x_{i+1}]$, whose midpoints are given by $x_{i+1/2} = x_i + \dfrac{\Delta x}{2}$. Time is discretized using a step Δt, so that successive time levels satisfy $t_{n+1} = t_n + \Delta t$.

At each time level t_n, the numerical approximation $\mathbf{u}_i^n$ denotes the cell average of the numerical solution over the control cell C_i, and approximates the corresponding cell average of the exact solution. The scheme relies on a piecewise linear representation $\mathcal{L}_i(x,t)$ constructed over each cell, designed to approximate the exact solution $\mathbf{u}(x,t)$ in an average sense, namely

$$\mathbf{u}_i^n = \frac{1}{\Delta x}\int_{C_i} \mathcal{L}_i(x,t)\,dx \;\approx\; \frac{1}{\Delta x}\int_{C_i} \mathbf{u}(x,t)\,dx.$$

At time t_n, this reconstruction is expressed as

$$\mathcal{L}_i(x,t_n) = \mathbf{u}_i^n + (x - x_i)\left(\mathbf{u}_i^n\right)', \qquad x \in C_i,$$

where the slope $\left(\mathbf{u}_i^n\right)'$ is a limited approximation of the spatial derivative $\partial \mathbf{u}/\partial x(x_i,t_n)$, computed using the Monotonized Central (MC)-θ limiter.

Throughout this section, $\mathbf{u}_i^n$ denotes the cell average over the primal cell C_i at time t_n, while $\mathbf{u}_{i+1/2}^n$ denotes the corresponding cell average over the dual cell $D_{i+1/2}$. The notation $\mathcal{L}_i(x,t)$ represents the local piecewise linear reconstruction over cell C_i, and the associated slopes correspond to the reconstructed spatial derivatives used in the forward projection, predictor, and backward projection steps.

We begin the construction of the numerical scheme by integrating the balance law (2.1) over the space–time domain $\gamma = D_{i+1/2} \times [t_n, t_{n+1}] = [x_i, x_{i+1}] \times [t_n, t_{n+1}]$ as follows:

$$\int\!\!\int_\gamma \left[\mathbf{u}_t + f(\mathbf{u})_x\right] dR = \int\!\!\int_\gamma S(\mathbf{u}, x)\, dR. \tag{2.3}$$

Applying Green's theorem to the left-hand side of (2.3), followed by the use of midpoint quadrature in both space and time, we obtain the evolution of $\mathcal{L}_i(x,t_n)$ onto the dual cell $D_{i+1/2}$ at the time level $n+1$, denoted $\mathbf{u}_{i+1/2}^{n+1}$:

$$\mathbf{u}_{i+1/2}^{n+1} = \mathbf{u}_{i+1/2}^n - \frac{\Delta t}{\Delta x}\Big[f\left(\mathbf{u}_{i+1}^{n+1/2}\right) - f\left(\mathbf{u}_i^{n+1/2}\right)\Big] + \frac{1}{\Delta x}\int_{t_n}^{t_{n+1}}\int_{x_i}^{x_{i+1}} S(\mathbf{u}, x)\, dx\, dt. \tag{2.4}$$

Approximating the source integral using midpoint quadrature and centered differences, it then becomes

$$\int_{t_n}^{t_{n+1}} \int_{x_i}^{x_{i+1}} S\,(\mathbf{u}, x)\; dx\, dt \approx \Delta t \Delta x \begin{pmatrix} 0 \\ -g \dfrac{h_{i+1}^{n+1/2} + h_i^{n+1/2}}{2} \dfrac{b_{i+1} - b_i}{\Delta x} \end{pmatrix}. \tag{2.5}$$

Then (2.4) can be written as

$$\mathbf{u}_{i+1/2}^{n+1} = \mathbf{u}_{i+1/2}^{n} - \frac{\Delta t}{\Delta x}\Big[f\left(\mathbf{u}_{i+1}^{n+1/2}\right) - f\left(\mathbf{u}_{i}^{n+1/2}\right)\Big] + \Delta t S\left(\mathbf{u}_{i}^{n+1/2}, \mathbf{u}_{i+1}^{n+1/2}\right), \tag{2.6}$$

where $S\left(\mathbf{u}_{i}^{n+1/2}, \mathbf{u}_{i+1}^{n+1/2}\right)$ approximates the source term with second-order accuracy as follows:

$$S\left(\mathbf{u}_{i}^{n+1/2}, \mathbf{u}_{i+1}^{n+1/2}\right) = \begin{pmatrix} 0 \\ -g \dfrac{h_{i+1}^{n+1/2} + h_i^{n+1/2}}{2} \left(\dfrac{b_{i+1} - b_i}{\Delta x}\right) \end{pmatrix}. \tag{2.7}$$

The forward projection of the primal cell averages $\mathbf{u}_i^n$ on the staggered grid at the same time t_n, $\mathbf{u}_{i+1/2}^n$, can be computed from the two neighboring control cells

$$\mathbf{u}_{i+1/2}^n = \frac{\mathbf{u}_{i+1/4}^n + \mathbf{u}_{i+3/4}^n}{2}, \tag{2.8}$$

where $\mathbf{u}_{i+1/4}^n = \dfrac{1}{\Delta x/2} \displaystyle\int_{x_i}^{x_{i+1/2}} \mathcal{L}_i(x,t)\, dx$, and $\mathbf{u}_{i+3/4}^n$ follows in turn. This leads to

$$\mathbf{u}_{i+1/2}^n = \frac{1}{2}\left(\mathbf{u}_i^n + \mathbf{u}_{i+1}^n\right) + \frac{\Delta x}{8}\left((\mathbf{u}_i^n)' - (\mathbf{u}_{i+1}^n)'\right). \tag{2.9}$$

Next, we compute the predicted solution values $\mathbf{u}_i^{n+1/2}$ via a first-order Taylor expansion in time together with the balance law (2.1) as follows:

$$\mathbf{u}_i^{n+1/2} = \mathbf{u}_i^n + \frac{\Delta t}{2}\Big[-(f(\mathbf{u}_i^n))' + S_i^n \Big], \tag{2.10}$$

where $(f(\mathbf{u}_i^n))' = J \cdot \left(\mathbf{u}_i^n\right)'$ and $J = \partial f / \partial \mathbf{u}$ is the Jacobian matrix of the system (2.1).

The source term is discretized following the approach introduced in [4], where it is decomposed into left, central, and right contributions $S_i^n = S_{i,L}^n + S_{i,C}^n + S_{i,R}^n$. For completeness, we only recall the left contribution, which corresponds to the case where the spatial derivative is approximated using a backward difference, while the full details can be found in [4]. It is given by

$$S_{i,L}^n = \alpha_L(s_i) \begin{pmatrix} 0 \\ -g h_i^n \theta \dfrac{b_i - b_{i-1}}{\Delta x} \end{pmatrix}, \tag{2.11}$$

where the coefficient $\alpha_L(s_i)$ depends on the slope selection parameter s_i, and $1 \leq \theta \leq 2$, as defined in [4].

Finally, the necessary backward projection of $\mathbf{u}_{i+1/2}^{n+1}$ on the original control grid at the time t_{n+1}, $\mathbf{u}_i^{n+1}$ can be computed similarly to (2.9), and thus reads

$$\mathbf{u}_i^{n+1} = \frac{1}{2}\left(\mathbf{u}_{i-1/2}^{n+1} + \mathbf{u}_{i+1/2}^{n+1}\right) + \frac{\Delta x}{8}\left(\left(\mathbf{u}_{i-1/2}^{n+1}\right)' - \left(\mathbf{u}_{i+1/2}^{n+1}\right)'\right). \tag{2.12}$$

In general, most numerical schemes fail to preserve the C-property in steady-state shallow water simulations. This issue arises in the context of central schemes because the bottom topography and the free surface are reconstructed as linear profiles over the control cells C_i, while this representation is not consistently maintained on the staggered cells $D_{i+1/2}$. As a result, a suitable modification of the scheme was introduced in [4], where the authors used the surface gradient formulation, expressing the discrete slope of the water height in terms of the free surface elevation $H(x, t)$.

Unlike path-conservative formulations, the present approach does not discretize nonconservative products through path integrals. Instead, equilibrium preservation is achieved through a compatible sensor-based coupling between the reconstructed free surface and the source term discretization. Consequently, the method retains the simplicity of the central finite-volume framework while ensuring preservation of the C-property.

Following [4], we consider the bottom topography to be specified at the cell interfaces, i.e., the values $b_{i+1/2}$ are given at the points $x_{i+1/2}$. Under this setting, the function $b(x)$ within each control cell C_i is reconstructed through linear interpolation as $b(x) = b_i + \frac{1}{\Delta x}\left(b_{i+1/2} - b_{i-1/2}\right)(x - x_i)$, where, at the cell centers x_i, we have

$$b_i = \frac{1}{2}\left(b_{i+1/2} + b_{i-1/2}\right). \tag{2.13}$$

The reconstruction of the water height $h(x)$ within each control cell is performed indirectly by first reconstructing the water surface elevation $H(x)$ and then using the identity $h(x) = H(x) - b(x)$. More specifically, the linear representation $H(x) = H_i + H_i'(x - x_i)$ over the cell C_i is obtained by applying a limiting procedure to the discrete gradients of $H_i = h_i + b_i$. To reconstruct the water height on the dual cells, an analogous procedure is applied. In this setting, the water surface at the staggered nodes is given by $(H_{i+1/2})_{\text{SGM}} = h_{i+1/2} + \hat{b}_{i+1/2}$, where

$$\hat{b}_{i+1/2} = b_{i+1/2} - \frac{1}{2}\left(b_{i+1/2} - \frac{b_i + b_{i+1}}{2}\right) \tag{2.14}$$

represents a corrected bottom value introduced to account for linearization of the topography $b(x)$ within the cell $D_{i+1/2}$. The corresponding approximation of the water height gradients over the control and dual cells, $(h_\ell)'_{\text{SGM}}$, $\ell = i, i + 1/2$, is given in [4] by using the surface gradient method, namely

$$(h_\ell)'_{\text{SGM}} = (H_\ell)'_{\text{SGM}} - \frac{1}{\Delta x}\Delta b_\ell, \qquad \forall \ell = i,\ i + \frac{1}{2}, \tag{2.15}$$

where Δb_ℓ denotes the corresponding discrete bottom variation, namely

$$\Delta b_i = b_{i+1/2} - b_{i-1/2}, \qquad \Delta b_{i+1/2} = b_{i+1} - b_i.$$

In order to ensure positivity, we incorporate a nonlinear limiter [15] into the abovementioned well-balanced unstaggered central scheme [4]. This reconstruction is used to adjust the preliminary slopes near wet–dry fronts whenever necessary. It requires

$$h_\ell \geq 0 \quad \Longrightarrow \quad h_\ell \pm \beta \Delta h_\ell \geq 0, \qquad \forall \ell = i,\ i + \frac{1}{2},$$

where $\beta \geq \frac{1}{2}$ is a parameter. The corresponding modification is given by

$$h'_\ell = \max\left(\min\left((h_\ell)'_{\text{SGM}}, \frac{h_\ell}{\beta\Delta x}\right), -\frac{h_\ell}{\beta\Delta x}\right), \qquad \forall \ell = i,\, i+\frac{1}{2}. \tag{2.16}$$

This correction prevents the reconstructed water depth from becoming negative and thus provides a natural mechanism for the treatment of wet–dry regions. The slopes h'_ℓ are obtained by applying the limiter (2.16) to the preliminary reconstruction $(h_\ell)'_{\text{SGM}}$, for all $\ell = i,\, i+\frac{1}{2}$. These limited slopes are used in the forward projection (2.9) and the backward projection (2.12), respectively.

We now recall the positivity mechanism associated with the IRP reconstruction. Let λ_i^n denote the maximum local wave speed computed from the reconstructed values at time t_n, and let $\lambda_{i+1/2}^{n+1/2}$ denote the corresponding maximum wave speed at the staggered half-time level. Following the positivity analysis in [15], the CFL condition is taken in the form

$$\frac{\Delta t}{\Delta x}\max_i\left\{\lambda_i^n, \lambda_{i+1/2}^{n+1/2}\right\} \leq \text{CFL}_\beta := \frac{\sqrt{3-\dfrac{1}{2\beta}}-1}{2}, \qquad \beta \geq \frac{1}{2}. \tag{2.17}$$

Under this condition, the IRP limiter (2.16) yields non-negative reconstructed values at the relevant quadrature and projection points. More precisely, the forward projection, the predictor step, the staggered update, and the backward projection can be written, for the water height component, as convex combinations of non-negative reconstructed quantities, as in the positivity proof of [15]. Since the source term of the shallow water system has a zero first component, the well-balanced source discretization used in the present scheme does not alter the height positivity argument. Therefore, away from the special lake-at-rest wet–dry correction introduced below, the standard IRP-limited update preserves non-negative water heights under the abovementioned CFL restriction.

Lemma 1 (Cutoff criteria for the nonlinear limiter)**.** *Consider the nonlinear limiter* (2.16) *in a fully wet region. The limiter is inactive, that is,* $h'_\ell = (h_\ell)'_{SGM}$, *if and only if* $h_\ell \geq \beta\Delta x\,\left|(h_\ell)'_{SGM}\right|$. *In particular, in the lake-at-rest case, this yields the unified cutoff condition*

$$h_\ell \geq \beta\left|\delta_\ell b\right| \qquad \textit{for all } \ell,$$

where

$$\delta_\ell b = \begin{cases} b_{i+\frac{1}{2}} - b_{i-\frac{1}{2}}, & \textit{if } \ell = i, \\ b_{i+1} - b_i, & \textit{if } \ell = i+\frac{1}{2}. \end{cases}$$

For fully flooded domains, and under the cutoff conditions given in Lemma 1, the numerical scheme can accurately reproduce stationary solutions up to machine precision. More precisely, the reconstructed slopes lie within the admissible bounds of the limiter; as a result, the scheme reduces locally to the original well-balanced formulation, for which the C-property was established in [14]. It follows that the proposed scheme preserves the lake-at-rest equilibrium. In particular, if the initial data correspond to such a configuration, then the numerical solution remains unchanged under the proposed scheme. Indeed, if $\mathbf{u}_i^n$ denotes the numerical solution at time $t = t_n$, after one time step, the scheme satisfies $\mathbf{u}_i^{n+1} = \mathbf{u}_i^n$, throughout the computational domain, with the intermediate and staggered updates also preserving the state, namely $\mathbf{u}_i^{n+1/2} = \mathbf{u}_i^n$ and $\mathbf{u}_{i+1/2}^{n+1} = \mathbf{u}_{i+1/2}^n$.

The cutoff condition in Lemma 1 also highlights a practical limitation of applying the nonlinear limiter uniformly throughout the computational domain. In fully wet regions with a relatively small water height compared with the local bottom variation, the cutoff condition may fail, causing the limiter to become active even though positivity is not at risk. In such situations, the reconstruction may be unnecessarily modified, which can degrade the original well-balanced discretization and lead to oscillatory behavior, particularly near steep or discontinuous bottom topographies.

In practice, it is convenient to activate the nonlinear limiter dynamically only in the vicinity of wet–dry transitions, thereby minimizing unnecessary restrictions on the water height relative to the steepness of the bottom topography as required in Lemma 1.

The discussion above shows that the limiter (2.16) provides the positivity mechanism for the standard wet–dry update, while the cutoff criterion in Lemma 1 ensures that, in sufficiently wet lake-at-rest regions, the limiter remains inactive and the original well-balanced formulation is recovered. However, this mechanism alone does not address the case of a lake-at-rest state containing dry regions, such as an emerging island. In that case, the wet–dry interface must also preserve the discrete equilibrium structure. This configuration is treated separately in the next subsection.

2.2. *Lake-at-rest property in the wet–dry case*

Another central contribution of the present work is the development of a tailored numerical treatment for lake-at-rest configurations in the presence of wet–dry interfaces. This correction is dynamically activated when the initial conditions feature a lake-at-rest state adjacent to a dry region. For such configurations, the mesh is set up in such a way that the waterfront coincides with the center of a dual cell, namely at the point $x_{i+1/2}$.

Consider a lake-at-rest configuration adjacent to a dry region, with the wet–dry interface located at the dual-cell center $x_{i+1/2}$. The wet region is characterized by a constant water surface level $H = h + b$ and zero velocity, while the neighboring cells on the dry side satisfy $h = 0$. Such a configuration is identified through a local discrete condition. For the representative case considered in this section, where the wet lake-at-rest region lies to the left of the interface and the dry region lies to the right, and taking into account the stencil of the numerical domain of dependence, this configuration can be characterized as

$$h_l + b_l = \text{constant for } i - 2 \leq l \leq i \quad \text{and} \quad h_l = 0 \text{ for } i + 1 \leq l \leq i + 3. \tag{2.18}$$

Remark 1. The detection criterion (2.18) is designed for discrete lake-at-rest wet–dry configurations. For problems involving a lake-at-rest state adjacent to a dry region, the wet–dry interface is first identified as the point separating the wet and dry regions, and the computational mesh is chosen so that this interface coincides with a dual-cell center $x_{i+1/2}$.

The algorithm monitors the local stencil around the wet–dry interface using a tolerance of 10^{-9}. The special correction is activated only when the local stencil satisfies the following two conditions:

(i) The cells on one side of the interface satisfy the discrete lake-at-rest relation $h + b = K$ with zero velocity;

(ii) The neighboring cells on the other side are dry.

For the representative configuration considered in (2.18), this corresponds to three cells on the wet side satisfying the lake-at-rest condition and three cells on the dry side.

Under these conditions, the special correction is applied and the C-property established in Theorem 1 guarantees preservation of the lake-at-rest state, so that the wet–dry interface remains stationary.

Whenever the local stencil no longer satisfies this detection criterion, the special correction is deactivated and the update is performed using the numerical scheme with a nonlinear limiter, treating the problem as a general wet–dry flow.

Other wet–dry configurations follow analogously. Figure 1 illustrates the configuration considered in this section, namely a lake-at-rest state to the left of the interface and a dry region to the right over a positively sloped bottom topography, with the waterfront falling exactly at the point $x_{i+1/2}$.

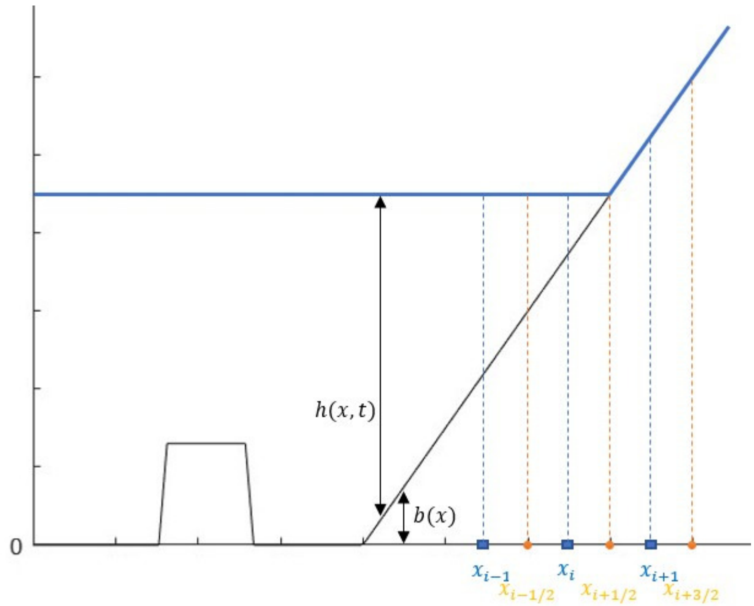

Figure 1. Representative lake-at-rest wet–dry configuration. The interface is located at $x_{i+1/2}$. The wet region (to the left of the interface) satisfies $u = 0$ and $H = h + b =$ constant, while the dry region (to the right of the interface) corresponds to $h = 0$ over a positively sloped bottom topography.

To advance the numerical solution in time and compute $\mathbf{u}^{n+1}_{i+1/2}$, we integrate the balance law (2.1) as shown in (2.3) to obtain the finite volume method defined by Eq (2.4).

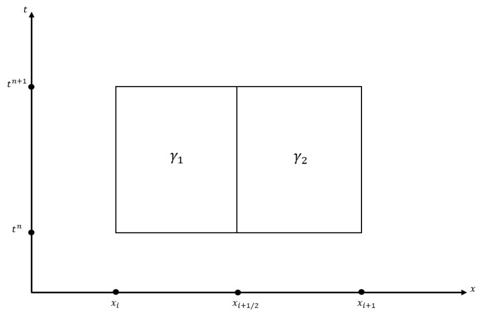

(a) Decomposition of the space–time control volume into the wet region γ_1 and the dry region γ_2.

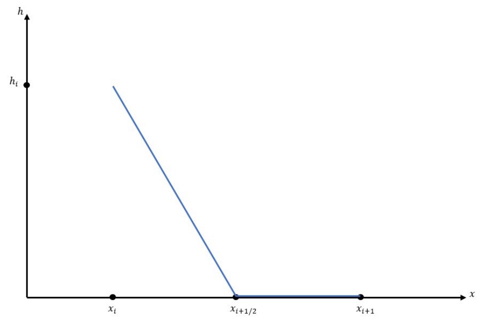

(b) Piecewise linear reconstruction near a wet–dry interface, with $h = 0$ in the dry region.

Figure 2. Illustration of the wet–dry treatment at $x_{i+1/2}$. The space–time control volume is divided into wet and dry regions, and the reconstructed water height vanishes over the dry portion of the cell.

At a wet–dry interface, the water height function is piecewise linear over the dual cell, as illustrated in Figure 2(b). Accordingly, the source term integral can be naturally decomposed over the wet and dry regions γ_1 and γ_2, shown in Figure 2(a). Moreover, the water height vanishes over the interval $[x_{i+1/2}, x_{i+1}]$. Because the water is either at rest or absent in the direct vicinity of the interface, the contribution of the source term over γ_2 vanishes, yielding

$$\iint_{\gamma} S(\mathbf{u}, x)\, dR = \iint_{\gamma_1} S(\mathbf{u}, x)\, dR.$$

Approximating the source term integral using midpoint quadrature and centered differences gives

$$\int_{t_n}^{t_{n+1}} \int_{x_i}^{x_{i+1/2}} S(\mathbf{u}, x)\, dx\, dt \approx \Delta t \frac{\Delta x}{2} \begin{pmatrix} 0 \\ -g \dfrac{h_{i+1/2}^{n+1/2} + h_i^{n+1/2}}{2} \dfrac{\hat{b}_{i+1/2} - b_i}{\Delta x/2} \end{pmatrix}, \tag{2.19}$$

where $\hat{b}_{i+1/2}$ is defined later in (2.22). Consequently, Eq (2.4) becomes

$$\mathbf{u}_{i+1/2}^{n+1} = \mathbf{u}_{i+1/2}^{n} - \frac{\Delta t}{\Delta x}\Big[f(\mathbf{u}_{i+1}^{n+1/2}) - f(\mathbf{u}_{i}^{n+1/2})\Big] + \Delta t \mathbf{S}_{i+1/2}^{WD}, \tag{2.20}$$

where

$$\mathbf{S}_{i+1/2}^{WD} = \begin{pmatrix} 0 \\ -g \dfrac{h_{i+1/2}^{n+1/2} + h_i^{n+1/2}}{4} \dfrac{\hat{b}_{i+1/2} - b_i}{\Delta x/2} \end{pmatrix}. \tag{2.21}$$

We now define the quantities $\mathbf{u}_{i+1/2}^{n}$, $\mathbf{u}_{i}^{n+1/2}$, and $h_{i+1/2}^{n+1/2}$ required for the computation of the updated staggered solution $\mathbf{u}_{i+1/2}^{n+1}$.

The forward projected solution $\mathbf{u}_{i+1/2}^{n}$ is obtained analogously to the fully wet case using Eq (2.9). However, at the wet–dry interface, the corrected bottom value must be redefined as

$$\hat{b}_{i+1/2} = \frac{3}{4}\, b_{i+1/2} + \frac{1}{4}\, b_i, \tag{2.22}$$

in order to preserve the physical lake-at-rest equilibrium at the interface. More precisely, this definition ensures that the reconstructed water level satisfies

$$h^n_{i+1/2} + \hat{b}_{i+1/2} = k, \tag{2.23}$$

where k denotes the constant lake level.

Next, we determine the predicted values $\mathbf{u}_i^{n+1/2}$. Since the lake-at-rest region lies to the left of the interface, the bottom gradient is discretized using a backward difference. Consequently, the source contribution $S^{\,n}_{i,L}$ introduced in (2.11) is used, from which (2.10) follows.

To evaluate the source contribution $\mathbf{S}^{WD}_{i+1/2}$ defined in (2.21), we need to determine the predicted water height $h^{n+1/2}_{i+1/2}$. For this purpose, we consider the predictor step at the staggered interface, obtained, following the same predictor construction as in (2.10), by applying a first-order Taylor expansion in time together with the balance law (2.1). Using the adjusted bottom topography (2.22), we obtain

$$\mathbf{u}^{n+1/2}_{i+1/2} = \mathbf{u}^n_{i+1/2} + \frac{\Delta t}{2}\begin{pmatrix} 0 \\ -gh^n_{i+1/2}\left(\left(h^n_{i+1/2}\right)' + \hat{b}'_{i+1/2}\right)\end{pmatrix}.$$

Since the predictor correction affects only the momentum component, the water height remains unchanged, namely

$$h^{n+1/2}_{i+1/2} = h^n_{i+1/2}. \tag{2.24}$$

Therefore, the interface water height appearing in the source term remains unchanged under the lake-at-rest configuration.

Finally, we determine the backward projection $\mathbf{u}_i^{n+1}$ from $\mathbf{u}^{n+1}_{i+1/2}$. The momentum component is obtained directly from (2.12). For the first component of $\mathbf{u}_i^{n+1}$, we work with the water surface H rather than with the water height h. We first compute H_i^{n+1} and then recover the water height through

$$h_i^{n+1} = H_i^{n+1} - b_i.$$

Using (2.12), the water surface is evaluated as

$$H_i^{n+1} = \frac{1}{2}\left(H^{n+1}_{i-1/2} + H^{n+1}_{i+1/2}\right) + \frac{\Delta x}{8}\left((H^{n+1}_{i-1/2})' - (H^{n+1}_{i+1/2})'\right), \tag{2.25}$$

where $(H^{n+1}_{i+1/2})'$ is approximated using a backward difference, namely

$$(H^{n+1}_{i+1/2})' = \frac{H^n_{i+1/2} - H^n_{i-1/2}}{\Delta x}.$$

Since the interface separates a lake-at-rest region from a dry region, it is essential to preserve the dry state, namely

$$h^{n+1}_{i+1} = 0.$$

Applying (2.12) to the control cell C_{i+1} for the water surface gives

$$H^{n+1}_{i+1} = \frac{1}{2}\left(H^{n+1}_{i+1/2} + H^{n+1}_{i+3/2}\right) + \frac{\Delta x}{8}\left((H^{n+1}_{i+1/2})' - (H^{n+1}_{i+3/2})'\right). \tag{2.26}$$

Observe that $(H^{n+1}_{i+3/2})' = b'_{i+3/2}$ naturally in the dry region. Therefore, we impose

$$(H^{n+1}_{i+1/2})' = b'_{i+1/2},$$

when reconstructing in the dry region, so that the water surface remains aligned with the bottom topography.

Thus,

$$(H^{n+1}_{i+1/2})' = \begin{cases} [(H^{n+1}_{i+1/2})']^- = \dfrac{H^n_{i+1/2} - H^n_{i-1/2}}{\Delta x}, & \text{when computing } \mathbf{u}^{n+1}_i \text{ in the wet region,} \\ [(H^{n+1}_{i+1/2})']^+ = b'_{i+1/2}, & \text{when computing } \mathbf{u}^{n+1}_{i+1} \text{ in the dry region.} \end{cases}$$

Under the present wet–dry lake-at-rest configuration, the surface gradient reconstruction at the interface remains compatible with the admissible bounds of the nonlinear limiter (2.16) when $\beta = \frac{1}{2}$. In addition, the corrected bottom value $\hat{b}_{i+1/2}$ defined in (2.22) ensures that the reconstructed water level satisfies the equilibrium relation (2.23). Consequently, the staggered reconstruction remains consistent with the exact lake-at-rest equilibrium at the wet–dry interface while preserving the dry state in the neighboring dry region. To formalize these observations, we next consider the representative benchmark configuration used in the following analysis.

Before stating the main result, we emphasize that the following analysis concerns the representative benchmark configuration in which a stationary wet–dry interface coincides with the center of a dual cell. This configuration is commonly adopted in well-balanced benchmark problems to assess the exact preservation of lake-at-rest equilibria. The theorem establishes that under this geometric assumption, the proposed reconstruction and source term discretization exactly preserve the discrete equilibrium together with the dry state. The treatment of general moving wet–dry interfaces is discussed separately in the numerical methodology.

Theorem 1 (lake-at-rest steady-state at a wet–dry interface)**.** *Assume that the numerical solution corresponds to a lake-at-rest configuration with a wet–dry interface located at the dual-cell center $x_{i+1/2}$, satisfying the discrete condition* (2.18)*. We also assume that the constant lake-at-rest water level coincides with the bottom elevation at the wet–dry interface, that is*

$$k = b_{i+1/2}.$$

Under the proposed wet–dry reconstruction and discretization defined through (2.9), (2.10), (2.20), (2.25), and (2.26), and for $\beta = \frac{1}{2}$, the scheme preserves the lake-at-rest property, namely

$$\mathbf{u}^{n+1}_i = \mathbf{u}^n_i.$$

Moreover, the forward projection onto the staggered grid remains consistent with the exact equilibrium state

$$H^n_{i+1/2} = H(x_{i+1/2}, 0),$$

and the dry region is exactly preserved as follows:

$$h^{n+1}_{i+1} = 0.$$

Proof. We begin by showing that the forward projection onto the staggered grid remains consistent with the equilibrium state at the wet–dry interface. The first component of (2.9) reads

$$h^n_{i+1/2} = \frac{1}{2}\left(h^n_i + h^n_{i+1}\right) + \frac{\Delta x}{8}\left((h^n_i)' - (h^n_{i+1})'\right). \tag{2.27}$$

Over the wet cell C_i, the equilibrium relation $H^n_i = h^n_i + b_i = k$ implies $(H^n_i)' = 0$. Using the limiter (2.16) with $\beta = \frac{1}{2}$, together with (2.13), it follows that

$$(h^n_i)' = -\frac{1}{\Delta x}(b_{i+1/2} - b_{i-1/2}).$$

On the dry cell C_{i+1}, we have $h^n_{i+1} = 0$; therefore, $(h^n_{i+1})' = 0$.
Substituting these relations into (2.27) and using $b_{i+1/2} - b_{i-1/2} = 2\left(b_{i+1/2} - b_i\right)$ yields

$$h^n_{i+1/2} = \frac{1}{4}\, b_{i+1/2} - \frac{1}{4}\, b_i.$$

Combining this identity with the corrected bottom reconstruction (2.22), namely

$$\hat{b}_{i+1/2} = \frac{3}{4}\, b_{i+1/2} + \frac{1}{4}\, b_i,$$

we obtain

$$\begin{aligned} h^n_{i+1/2} + \hat{b}_{i+1/2} &= \left(\frac{1}{4}\, b_{i+1/2} - \frac{1}{4}\, b_i\right) + \left(\frac{3}{4}\, b_{i+1/2} + \frac{1}{4}\, b_i\right) \\ &= b_{i+1/2}. \end{aligned}$$

By the assumption of Theorem 1, we have $b_{i+1/2} = k$. Therefore, $h^n_{i+1/2} + \hat{b}_{i+1/2} = k$.
Consequently, we have

$$H^n_{i+1/2} = H(x_{i+1/2}, 0).$$

To establish the preservation of the lake-at-rest configuration, we prove the identities

$$\mathbf{u}^{n+1/2}_i = \mathbf{u}^n_i, \qquad \mathbf{u}^{n+1}_{i+1/2} = \mathbf{u}^n_{i+1/2}, \qquad \mathbf{u}^{n+1}_i = \mathbf{u}^n_i.$$

Using (2.10), together with the source contribution (2.11) corresponding to $s_i = -1$, we obtain

$$\begin{aligned} \mathbf{u}^{n+1/2}_i &= \mathbf{u}^n_i + \frac{\Delta t}{2}\Big[-(f(\mathbf{u}^n_i))' + S^n_i\Big] \\ &= \mathbf{u}^n_i + \frac{\Delta t}{2}\left[-\begin{pmatrix} 0 & 1 \\ gh^n_i & 0 \end{pmatrix}\begin{pmatrix} (h^n_i)' \\ 0 \end{pmatrix} + \begin{pmatrix} 0 \\ -gh^n_i\theta\dfrac{b_i - b_{i-1}}{\Delta x} \end{pmatrix}\right]. \end{aligned}$$

Since $(h^n_i)' = \theta(h^n_i - h^n_{i-1})/\Delta x$ and $h^n_i + b_i = h^n_{i-1} + b_{i-1} = k$, the flux gradient and source term exactly balance each other. Hence, we have

$$\mathbf{u}^{n+1/2}_i = \mathbf{u}^n_i.$$

Next, we consider the update of $\mathbf{u}^{n+1}_{i+1/2}$ at the wet–dry interface. In a lake-at-rest configuration, the water height profile across the dual cell is not globally linear: On the wet side, the water height is reconstructed linearly toward the interface, whereas on the dry side, it vanishes identically. Therefore, a standard linear reconstruction over the entire dual cell cannot preserve the equilibrium structure. For this reason, the wet–dry reconstruction is treated in a piecewise manner.

At the wet–dry interface, the contribution from the dry side vanishes identically, since both the water height and discharge are zero there. Consequently, the update reduces to the wet side's contribution only.

With these observations, and using (2.20) and (2.21), we obtain

$$\mathbf{u}^{n+1}_{i+1/2} = \mathbf{u}^{n}_{i+1/2} - \frac{\Delta t}{\Delta x}\left[\begin{pmatrix} 0 \\ \frac{1}{2}g\left(h^{n+1/2}_{i+1/2}\right)^2 \end{pmatrix} - \begin{pmatrix} 0 \\ \frac{1}{2}g\left(h^{n+1/2}_{i}\right)^2 \end{pmatrix}\right] + \Delta t \begin{pmatrix} 0 \\ -g\dfrac{h^{n+1/2}_{i+1/2} + h^{n+1/2}_{i}}{2}\dfrac{\hat{b}_{i+1/2} - b_i}{\Delta x} \end{pmatrix}.$$

Using $h^{n+1/2}_{i+1/2} = h^{n}_{i+1/2}$ and $h^{n+1/2}_{i} = h^{n}_{i}$, we obtain

$$\begin{aligned}
\mathbf{u}^{n+1}_{i+1/2} &= \mathbf{u}^{n}_{i+1/2} + \frac{g\Delta t}{2\Delta x}\begin{pmatrix} 0 \\ \left(h^n_i\right)^2 - \left(h^n_{i+1/2}\right)^2 - \left(h^n_{i+1/2} + h^n_i\right)\left(\hat{b}_{i+1/2} - b_i\right) \end{pmatrix} \\
&= \mathbf{u}^{n}_{i+1/2} + \frac{g\Delta t}{2\Delta x}\begin{pmatrix} 0 \\ \left(h^n_{i+1/2} + h^n_i\right)\left[h^n_i - h^n_{i+1/2} - \hat{b}_{i+1/2} + b_i\right] \end{pmatrix}.
\end{aligned}$$

Using the equilibrium relations

$$h^n_i + b_i = k, \qquad h^n_{i+1/2} + \hat{b}_{i+1/2} = k,$$

we obtain

$$h^n_i - h^n_{i+1/2} - \hat{b}_{i+1/2} + b_i = 0.$$

Therefore, we have

$$\mathbf{u}^{n+1}_{i+1/2} = \mathbf{u}^{n}_{i+1/2}.$$

Finally, the momentum component of $\mathbf{u}^{n+1}_i$ follows directly from (2.12). For the water height, we compute H^{n+1}_i from (2.25) and then use $h^{n+1}_i = H^{n+1}_i - b_i$. Since $H^{n+1}_{i-1/2} = H^{n+1}_{i+1/2} = k$ and $(H^{n+1}_{i+1/2})'$ is approximated by a backward difference, we have

$$(H^{n+1}_{i+1/2})' = \frac{H^n_{i+1/2} - H^n_{i-1/2}}{\Delta x} = 0.$$

Moreover, $(H^{n+1}_{i-1/2})' = 0$. Hence, (2.25) gives $H^{n+1}_i = k$, and therefore

$$h^{n+1}_i = H^{n+1}_i - b_i = k - b_i = h^n_i.$$

Thus

$$\mathbf{u}^{n+1}_i = \mathbf{u}^n_i.$$

The three identities above establish the preservation of the lake-at-rest configuration at the wet–dry interface.

Finally, we show that the dry state remains preserved. Since the cell C_{i+1} is initially dry, it is sufficient to prove that $H^{n+1}_{i+1} = H^n_{i+1}$.

Using (2.26), together with $(H^{n+1}_{i+1/2})' = (b_{i+1/2})'$ and $(H^{n+1}_{i+3/2})' = (b_{i+3/2})'$, the gradient contributions cancel since both coincide with the bottom slope. Hence

$$\begin{aligned} H^{n+1}_{i+1} &= \frac{1}{2}\left(H^{n+1}_{i+1/2} + H^{n+1}_{i+3/2}\right) \\ &= H^{n}_{i+1}. \end{aligned}$$

Therefore

$$h^{n+1}_{i+1} = 0,$$

and the dry region remains preserved. □

Remark 2. The wet–dry lake-at-rest correction also preserves non-negative water heights. Indeed, on the wet side of the interface, Theorem 1 gives $\mathbf{u}^{n+1}_i = \mathbf{u}^n_i$, and hence $h^{n+1}_i = h^n_i \geq 0$. On the dry side, the same theorem gives exact preservation of the dry state, namely $h^{n+1}_{i+1} = 0$. The reversed wet–dry configuration is treated analogously. Thus, the special lake-at-rest interface correction is consistent with the positivity-preserving mechanism of the full scheme.

3. Numerical experiments

In this section, we conduct a series of numerical experiments to assess the accuracy, robustness, and well-balancedness of the proposed numerical scheme. Unless otherwise stated, the gravitational constant is taken as $g = 9.8\,\mathrm{m/s^2}$. The time step Δt is dynamically computed at the beginning of each iteration according to the CFL restriction (2.17).

Unless otherwise stated, we use $\beta = \frac{3}{2}$ throughout the numerical experiments, corresponding to $\mathrm{CFL}_\beta \approx 0.3165$.

In practice, it was sufficient to compute the time step at each iteration using only the cell-centered wave speeds, namely

$$\Delta t = \frac{\mathrm{CFL}_\beta\, \Delta x}{\max_i \lambda^n_i}.$$

No loss of positivity was observed in any of the reported numerical experiments.

In what follows, we consider a number of standard benchmark problems from the literature.

The MC-θ limiter described earlier is used throughout all numerical experiments with $\theta = 1.5$, unless explicitly stated otherwise. In addition, a dry tolerance of $h_{\mathrm{dry}} = 10^{-5}$ is used to distinguish wet and dry states. During all simulations, the water height is monitored at every iteration, and a warning is triggered whenever a negative water height is detected. No negative water heights were observed in any of the reported experiments.

The main goal is to evaluate the performance of the proposed well-balanced unstaggered central scheme and, whenever relevant, to compare its results with those produced by the unstaggered central scheme with wet–dry treatment (UCS-WD) described in [14] and other reference solutions from the literature.

3.1. Accuracy test

We first consider the smooth benchmark problem from [11] to assess the numerical accuracy of the proposed method. The bottom topography is defined by

$$b(x) = \sin^2(\pi x)$$

over the computational domain $[0, 1]$, with periodic boundary conditions.

The initial water depth and discharge are prescribed by

$$h(x, 0) = 5 + e^{\cos(2\pi x)}, \qquad hu(x, 0) = \sin(\cos(2\pi x)).$$

The simulation is performed on successively refined uniform grids ranging from 50 to 800 cells up to the final time $t = 0.1$. To reduce the influence of temporal discretization on the observed convergence rates, the parameter β is decreased as the mesh is refined, resulting in progressively smaller effective CFL numbers.

The errors are computed using a self-convergence procedure, where each numerical solution is compared with the solution on the next refined grid after restriction to the coarser grid. Table 1 reports the corresponding L_1 errors for both h and hu, together with the observed orders of convergence.

Table 1. Accuracy test: L_1 errors and corresponding experimental orders of convergence (EOC) for h and hu at the final time $t = 0.1$ under different values of β and effective CFL numbers.

No. of cells	β	CFL_β	$L_1(h)$	Order	$L_1(hu)$	Order
50	1.50	0.3165	1.0955e-02	–	7.5512e-02	–
100	1.25	0.3062	2.3281e-03	2.23	1.8294e-02	2.05
200	1.00	0.2906	5.7049e-04	2.03	4.4167e-03	2.05
400	0.75	0.2638	1.5157e-04	1.91	1.1444e-03	1.95

The reported convergence rates in Table 1 indicate second-order numerical accuracy for both the water height and discharge in this smooth benchmark problem.

3.2. Lake at rest with two wet–dry interfaces

We next consider a problem that features a stationary configuration involving a lake at rest with two wet–dry interfaces located on two inclined ramps. This test is particularly relevant for verifying the capability of our proposed numerical scheme to preserve equilibrium states in the presence of dry areas.

The bottom topography is given by

$$b(x) = \begin{cases} -4.5(x + 2.5), & x \le -2.5, \\ 0, & -2.5 < x < 0, \\ 4x, & x \ge 0. \end{cases}$$

The initial water height is prescribed by

$$h(x, 0) = \max(k - b(x), 0),$$

with $k = 4.5$, while the initial velocity is set to zero, $u(x, 0) = 0$.

The computational domain we consider is the interval $[-5, 3]$, which we discretize using 200 cells, resulting in a spatial step size $\Delta x = 0.04$. The numerical solution is evaluated at time $t = 1$.

For this lake-at-rest benchmark with wet–dry interfaces, we use $\beta = \frac{1}{2}$, as discussed in Section 2.2. This corresponds to $\mathrm{CFL}_\beta \approx 0.2071$. Free boundary conditions are imposed at both boundaries. The wet–dry correction is activated according to the detection criterion introduced in (2.18).

The results illustrated in Figure 3 indicate that the numerical solution, computed at the final time, preserves the lake-at-rest configuration up to machine precision, thus confirming the exact well-balanced property of the proposed method. In addition, no negative water height values were observed throughout the simulation, confirming the positivity-preserving behavior of the proposed numerical scheme under the CFL condition adopted in the computations.

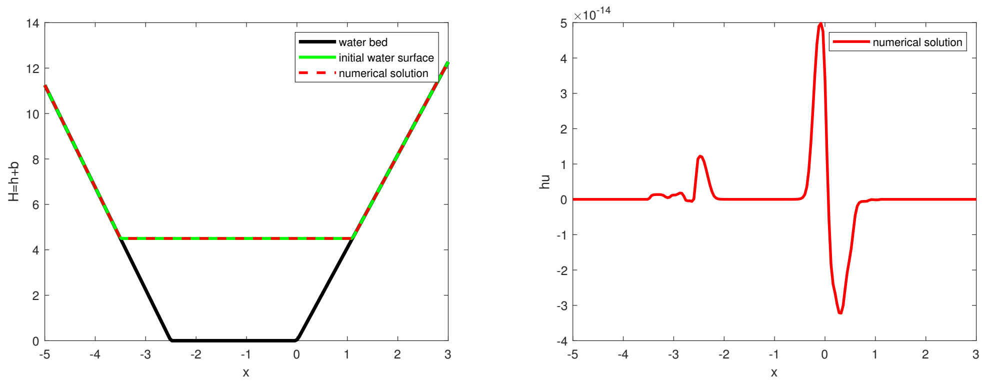

(a) Water surface $H = h + b$ at $t = 0$ and $t = 1$. **(b)** Momentum hu at $t = 1$.

Figure 3. Problem 2: lake-at-rest configuration with two wet–dry interfaces. The left panel shows the initial and final water surface profiles $H = h + b$ at $t = 0$ and $t = 1$, respectively. The right panel shows the corresponding momentum profile hu at the final time $t = 1$.

To further confirm the robustness of the solver, we compute the solution using double-precision arithmetic and report the corresponding L_1 errors in Table 2. The results confirm that the numerical solution matches the initial steady-state configuration up to machine accuracy. In particular, the computed errors remain at the level of round-off errors, indicating that the proposed scheme preserves the steady state without introducing spurious numerical perturbations or other nonphysical behavior.

Table 2. L_1 errors for the lake-at-rest configuration with two wet–dry interfaces.

No. of cells	h	hu
200	3.69e-16	2.88e-14

3.3. Perturbation of a lake-at-rest problem with wet–dry interfaces

In this test case, we introduce a perturbation to the lake-at-rest problem we solved in Problem 3.2. Such a problem simultaneously features a propagating wave from the center of the domain towards the dry and inclined boundaries. More precisely, it combines moving fronts with a nontrivial topography and therefore provides a further test of the robustness of the proposed method.

The bottom topography is given by

$$b(x) = \begin{cases} -4.5(x+2.5), & x \le -2.5, \\ 0, & -2.5 < x < 0, \\ 4x, & x \ge 0. \end{cases}$$

We define the initial water height as

$$h(x,0) = \begin{cases} 7 - b(x), & -2 \le x \le -1.5, \\ \max\left(k - b(x), 0\right), & \text{otherwise}, \end{cases}$$

where $k = 4.5$. The initial velocity is taken to be zero, with $u(x,0) = 0$.

The computational domain is the interval $[-5, 3]$, which we discretize using 200 cells, so that $\Delta x = 0.04$. The numerical solution is generated using the proposed numerical scheme, and the results obtained at time $t = 1$ are reported in Figure 4.

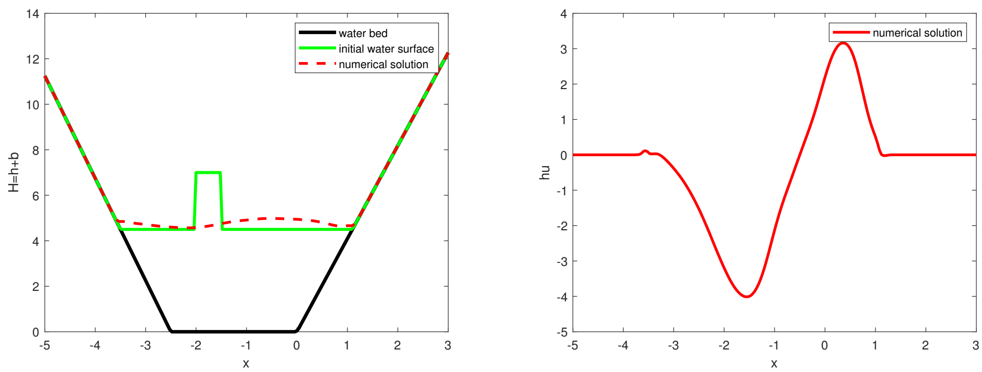

(a) Water surface $H = h + b$ at $t = 0$ and $t = 1$. **(b)** Momentum hu at $t = 1$.

Figure 4. Problem 3: Perturbation of a lake-at-rest problem with wet–dry interfaces. The left panel shows the initial and final water surface profiles $H = h + b$ at $t = 0$ and $t = 1$, respectively. The right panel shows the corresponding momentum profile hu at the final time $t = 1$.

The same free boundary conditions as in Problem 3.2 are imposed at both boundaries. The wet–dry lake-at-rest correction is applied only in the cells satisfying the detection criterion (2.18). When this local lake-at-rest condition is satisfied, the value $\beta = \frac{1}{2}$ is used, as described in Section 2.2. Once the perturbation breaks this local equilibrium condition, the computation switches to the general limited scheme described in Section 2.1, where $\beta = \frac{3}{2}$ is used. The corresponding CFL values are

$$\mathrm{CFL}_{1/2} \approx 0.2071, \qquad \mathrm{CFL}_{3/2} \approx 0.3165.$$

The relative mass conservation error at the final time $t = 1$ is computed as

$$\frac{|m(T) - m(0)|}{m(0)} = 1.2801 \times 10^{-5},$$

indicating that the proposed scheme preserves the total water mass with very good accuracy throughout the wet–dry evolution.

3.4. *Dam break over a discontinuous bottom: Wet domain*

We consider a wet-domain dam-break problem over a discontinuous bottom topography, adapted from the test case introduced in [4]. This benchmark provides a useful framework for evaluating the behavior of the numerical scheme near bottom discontinuities, where methods that are not well-balanced are known to generate spurious oscillations. To investigate the influence of the cutoff condition stated in Lemma 1, three different configurations of the initial water height are examined. The bottom profile is fixed and given by

$$b(x) = \begin{cases} 3, & |x - 600| < 300, \\ 0, & \text{otherwise.} \end{cases}$$

We then prescribe three different initial water height distributions. In the first case, both water levels are below the cutoff value, namely

$$h(x,0) = \begin{cases} 5 - b(x), & x < 600, \\ 4 - b(x), & x \geq 600. \end{cases}$$

In the second case, only one of the two water levels satisfies the cutoff condition, namely

$$h(x,0) = \begin{cases} 6 - b(x), & x < 600, \\ 5 - b(x), & x \geq 600. \end{cases}$$

Finally, in the third case, both water levels satisfy the cutoff condition, namely

$$h(x,0) = \begin{cases} 7 - b(x), & x < 600, \\ 6 - b(x), & x \geq 600. \end{cases}$$

In all three cases, the initial velocity is taken to be zero. The computational interval $[0, 1200]$ is discretized using 400 cells, and the numerical solution is computed up to the final time $t = 20$. The purpose of these three configurations is to show the effect of the cutoff value on the numerical behavior of the scheme.

Free boundary conditions are imposed at both boundaries and implemented by linear extrapolation in the ghost cells. Since this is a fully wet-domain test, the lake-at-rest wet–dry detection criterion (2.18) is not satisfied; therefore, the special lake-at-rest wet–dry treatment described in Section 2.2 is not activated. Consequently, the computation is governed by the general limited scheme described in Section 2.1.

For comparison, both the proposed scheme and the UCS-WD scheme are computed under identical numerical settings, including the same computational domain, grid resolution, CFL number, boundary conditions, and bottom discretization. Therefore, any differences in the numerical results are solely due to the different reconstruction and limiting mechanisms used by the two schemes.

Figure 5(a) displays the three initial water-height configurations considered in this test, corresponding, respectively, to cases where the cutoff condition from Lemma 1 is satisfied on both sides (solid red with markers), satisfied on only one side (solid magenta with markers), and violated on both sides (solid green with markers).

Figure 5(b) shows that when the cutoff condition is satisfied, the proposed scheme (solid red with markers) produces a smooth oscillation-free solution near the bottom discontinuities, while the UCS-WD scheme (solid blue) exhibits visible spurious oscillations. In Figure 5(c), only one side satisfies the cutoff condition; accordingly, the solution remains smooth on that side, whereas oscillations appear on the other side. Finally, Figure 5(d) corresponds to the case where the cutoff condition is violated on both sides, leading to stronger oscillatory behavior throughout the solution. These results highlight the importance of the cutoff condition in preserving the expected well-balanced behavior of the scheme in fully wet regions.

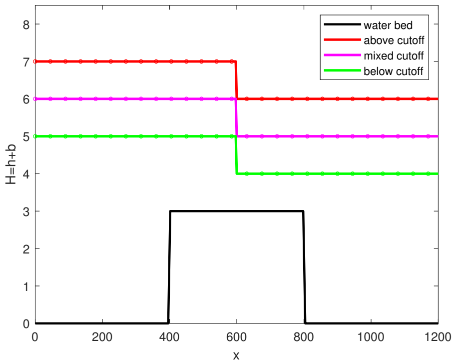

(a) Initial water surface profiles $H = h+b$ at $t = 0$ for the three configurations with $\beta = \frac{3}{2}$.

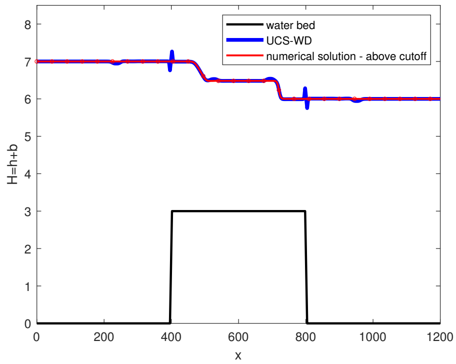

(b) Water surface profiles $H = h + b$ at $t = 20$: Cutoff-satisfying solution versus UCS-WD.

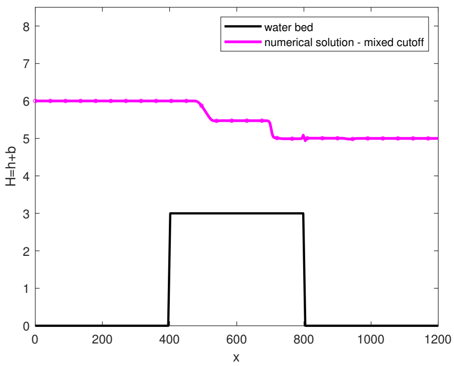

(c) Water surface profiles $H = h + b$ at $t = 20$: One-sided above-cutoff configuration.

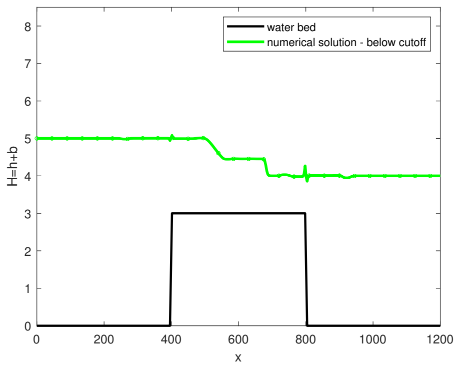

(d) Water surface profiles $H = h + b$ at $t = 20$: Double-sided below-cutoff configuration.

Figure 5. Problem 4: Effect of the cutoff condition from Lemma 1 on the wet-domain dam-break problem over a discontinuous bottom topography. The top-left panel shows the initial water surface profiles $H = h + b$ at $t = 0$ for the three considered configurations with $\beta = \frac{3}{2}$. The remaining panels display the computed water surface profiles at the final time $t = 20$ for different cutoff configurations.

The oscillations observed in the UCS-WD profiles are mainly attributed to differences in the reconstruction and limiting strategies of the two schemes. Although UCS-WD is positivity-preserving, it may lose the exact well-balanced property in fully wet regions when the reconstruction is unnecessarily modified, leading to significant oscillatory behavior. In contrast, under the cutoff conditions established in Lemma 1, the limiter in the proposed scheme remains inactive in sufficiently wet regions, allowing recovery of the original well-balanced discretization. As a result, the proposed scheme preserves both positivity and well-balancedness, yielding significantly improved and essentially oscillation-free profiles.

To further investigate the influence of the cutoff parameter, we performed a sensitivity study on the second configuration of Problem 4, corresponding to the one-sided above-cutoff case, where the cutoff condition from Lemma 1 is satisfied on one side of the discontinuity and violated on the other.

Figure 6 shows the numerical solutions obtained for three different values of β, namely $\beta = 2$, $\beta = \frac{3}{2}$, and $\beta = \frac{1}{2}$. The results confirm that larger values of β make the cutoff condition more restrictive, leading to more pronounced oscillations near the bottom discontinuity. On the other hand, smaller values of β relax the cutoff condition and reduce unnecessary activation of the nonlinear limiter in fully wet regions. In particular, for $\beta = \frac{1}{2}$, the solution remains essentially oscillation-free.

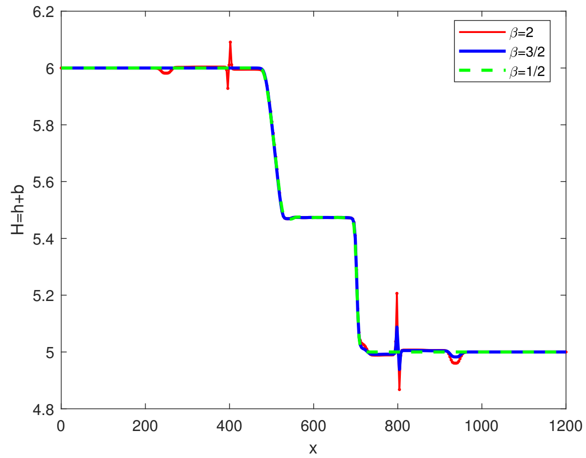

Figure 6. Problem 4: Sensitivity analysis with respect to β for the one-sided above-cutoff configuration. Water surface profiles $H = h + b$ at $t = 20$ are shown for $\beta = 2$, $\beta = \frac{3}{2}$, and $\beta = \frac{1}{2}$.

3.5. *Parabolic bowl*

This benchmark features a flow over a parabolic bottom profile for which an exact solution is available, redwhich was previously studied in [13]. It provides a standard test for assessing accuracy in the presence of wet–dry transitions.

The bottom topography, the initial condition (shown in Figure 7(a)), and the analytical solution follow the formulation in [13]. For completeness, we recall that the bottom has a parabolic shape, and the solution evolves within a bounded wet–dry region.

The computational domain is taken as $[-5000, 5000]$ and discretized using 200 uniform cells. The simulation is performed up to time $t = 500$.

Free boundary conditions are imposed at both boundaries and implemented by linear extrapolation in the ghost cells. Although this benchmark involves wet–dry transitions, the lake-at-rest wet–dry detection criterion (2.18) is not satisfied during the simulation. Therefore, the special treatment described in Section 2.2 is not activated, and the computation is governed by the general limited scheme described in Section 2.1.

For the comparison shown in Figure 7, both the proposed scheme and the UCS-WD scheme are run using exactly the same computational setup, including the same computational domain, the same uniform grid, the same boundary conditions, and the same bottom discretization. The time step for both schemes is selected using the same CFL-based stability condition. Therefore, the comparison is performed under identical numerical settings, ensuring that the observed differences arise solely from the distinct reconstruction and limiting strategies of the two schemes.

Figure 7(b) shows the water level $H = h + b$ at the final time. The analytical solution (solid light blue) serves as the exact reference, while the proposed method (dotted red) is compared with the UCS-WD scheme (dashed blue). Both numerical solutions are in very good agreement with the analytical profile, producing nearly indistinguishable results.

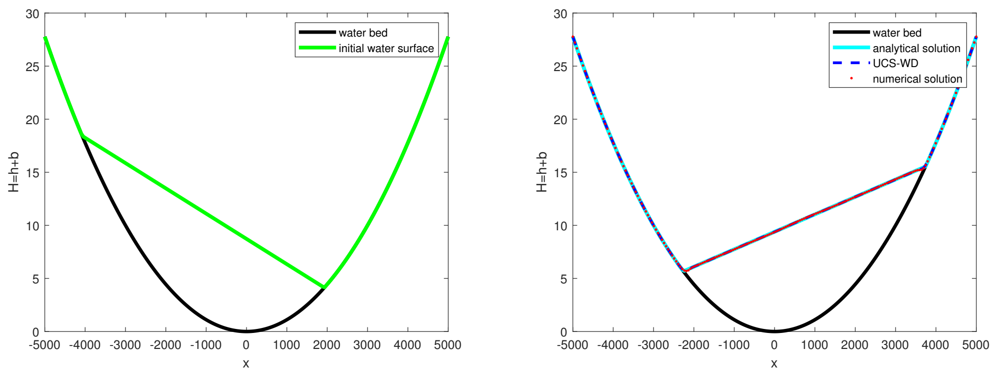

(a) Initial water surface profile $H = h + b$ at the initial time $t = 0$.

(b) Water surface profile $H = h + b$ at $t = 500$: Analytical and numerical solutions.

Figure 7. Problem 5: Parabolic bowl test. The left panel shows the initial water surface profile $H = h + b$ at $t = 0$. The right panel shows the water surface profile at $t = 500$, where the analytical solution (solid light blue) serves as the exact reference, while the proposed method (dotted red) is compared with the UCS-WD scheme (dashed blue).

The small oscillations observed in the comparison are mainly attributed to differences in the nonlinear reconstruction and the limiting strategies used by the two schemes, particularly near the moving wet–dry interface where the solution loses smoothness. Since the proposed method and UCS-WD use different reconstruction procedures near steep gradients and wet–dry fronts, slight local discrepancies are expected. Nevertheless, both schemes remain stable, preserve non-negative water heights, and accurately capture the analytical solution.

To provide a quantitative comparison for this benchmark, we computed the normalized L_1-error between the numerical and analytical water heights at the intermediate time $t = 300$. This time is chosen to assess the accuracy of the scheme during the main phase of the wet–dry evolution, before later-stage oscillatory effects associated with repeated drying and rewetting become more pronounced. The normalized error is defined by

$$L_1(h) = \frac{1}{|\Omega|}\Delta x \sum_i |h_i^{num} - h_i^{exact}|,$$

where $|\Omega|$ denotes the length of the computational domain. We also report the minimum computed water height over all cells and all time steps, denoted by $\min_{i,n} h_i^n$.

The results in Table 3 show clear convergence toward the analytical solution. The observed rates remain between first and second order, which is expected for a wet–dry benchmark where the solution is not globally smooth near the moving wet–dry interface. In all computations, the minimum water height remains equal to zero, confirming that no negative water depth was generated during the simulations and that dry regions were preserved without producing nonphysical values.

Table 3. Problem 5 (Parabolic bowl): Normalized L_1 errors, corresponding experimental orders of convergence (EOC), and minimum computed water height $\min_{i,n} h_i^n$.

No. of cells	$L_1(h)$	Order	$\min_{i,n} h_i^n$
200	1.0075e-02	–	0
400	3.4616e-03	1.54	0
800	1.1240e-03	1.62	0
1600	4.9000e-04	1.20	0

3.6. Vacuum occurrence by a double rarefaction wave over a step

This benchmark, adapted from [10], considers the formation of a dry region over a discontinuous bottom topography. It provides a challenging test for assessing the robustness of numerical schemes in the presence of discontinuous bathymetry, strong wave interactions, and vacuum formation.

The computational domain has a length of 25, and the bottom topography is defined by

$$b(x) = \begin{cases} 1, & \dfrac{25}{3} \le x \le 12.5, \\ 0, & \text{otherwise.} \end{cases}$$

The initial water surface is described by

$$h(x,0) + b(x) = 10,$$

while the initial discharge is given by

$$hu(x,0) = \begin{cases} 350, & x \le \dfrac{50}{3}, \\ -350, & \text{otherwise.} \end{cases}$$

The initial configuration drives the flow outward from the center of the domain, eventually producing a dry region near the discontinuous step.

The computational interval is discretized using 250 cells. Free boundary conditions are applied at both boundaries. The numerical solution is computed using the proposed scheme with $\beta = \frac{1}{2}$, corresponding to the smallest admissible value satisfying (2.17). This choice yields the most restrictive CFL condition within the present framework. For reference, the computations in [10] were performed using a CFL number of 0.08. For comparison, the benchmark setup is kept consistent with [10], including the same computational domain, initial condition, boundary conditions, and bottom topography. The main differences between the two computations arise from the numerical discretization and reconstruction framework: The reference method in [10] is based on a fifth-order well-balanced positivity-preserving WENO scheme, whereas the present method uses a second-order unstaggered central scheme with nonlinear limiting. The numerical results are reported at times $t = 0.05, 0.25$, and 0.65 in Figure 8.

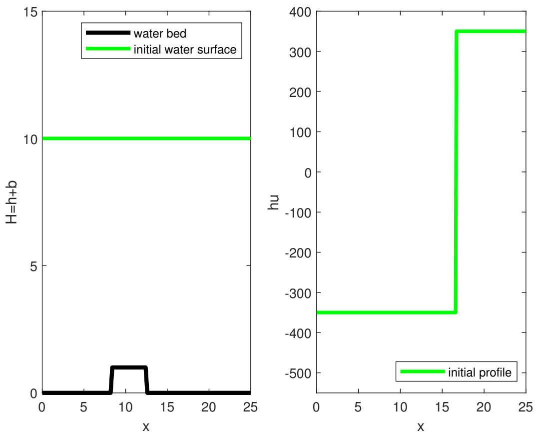

(a) Initial profiles at $t = 0$.

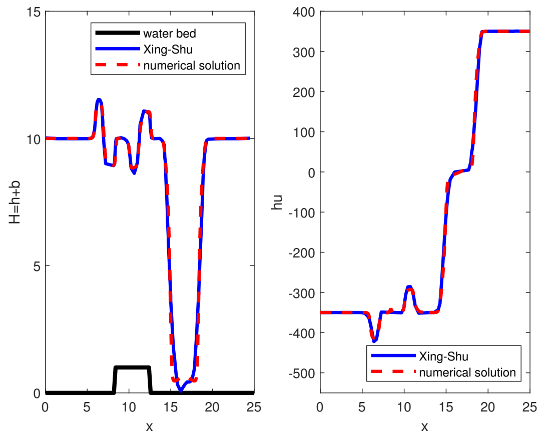

(b) Profiles at $t = 0.05$.

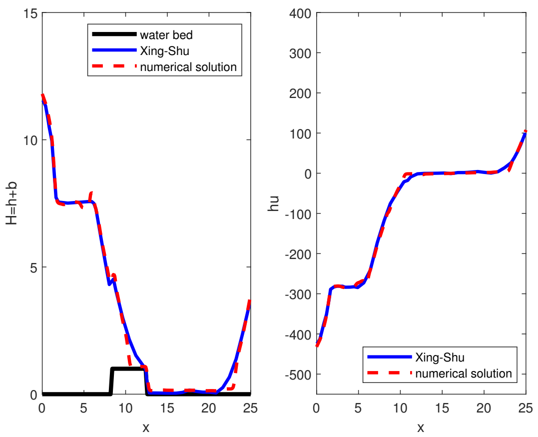

(c) Profiles at $t = 0.25$.

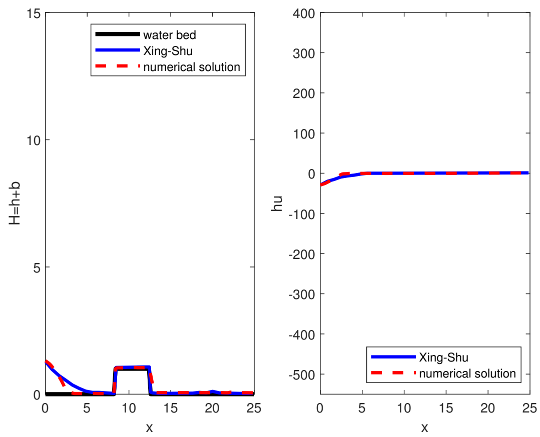

(d) Profiles at $t = 0.65$.

Figure 8. Problem 6: Vacuum occurrence by a double rarefaction wave over a step. The top left panel shows the initial water surface and discharge profiles at $t = 0$. The remaining panels display the numerical and reference solutions at times $t = 0.05, 0.25$, and 0.65. In each panel, the left subplot shows the water surface profile $H = h + b$, while the right subplot shows the discharge profile hu. The solid blue curves denote the reference solutions reported in [10], while the dashed red curves represent the numerical results obtained using the proposed scheme.

The comparison with the reference solutions reported in [10] shows that the proposed scheme successfully captures the main qualitative features of this benchmark, including the outward propagation of the flow, the formation of the dry region, and the overall wet–dry evolution over the discontinuous bottom topography.

Some visible discrepancies can be observed between the present results and the reference solutions. These discrepancies are primarily attributed to the substantial difference in the numerical accuracy and reconstruction framework of the two methods. In particular, the reference method in [10] is based on a fifth-order well-balanced positivity-preserving WENO scheme, whereas the present method is a second-order unstaggered central scheme. Due to this significant difference in formal order of accuracy, especially in the presence of a discontinuous bottom topography, strong rarefaction waves, and vacuum formation, exact agreement between the two solutions is not expected. Nevertheless, the proposed scheme remains stable, preserves non-negative water heights under the positivity-preserving reconstruction and the CFL condition stated in Section 2.1, and successfully captures the essential dynamics and qualitative behavior of this challenging benchmark.

3.7. *Flooding on a channel with two mounds*

In this test case, adapted from [26], we consider a flooding scenario in a channel with two bottom mounds. The objective is to evaluate the ability of the scheme to capture advancing wet fronts over a nontrivial topography starting from an initially dry bed. The channel has a length of 75, and the bottom profile is defined by

$$b(x) = \max\left(0, m_1(x), m_2(x)\right),$$

where

$$m_1(x) = 1 - 0.1\sqrt{(x-30)^2},$$
$$m_2(x) = 2.8 - 0.8\sqrt{(x-47.5)^2}.$$

Initially, the domain is dry, i.e., $h = hu = 0$. The right boundary is treated as an open outflow, while at the left boundary, an inflow condition is imposed with $u = 1$ and $h = 0.5$ for $t \leq 300$, and $h = 1$ for $t \geq 300$. The computational domain is discretized using 150 cells.

The numerical solution is computed using the proposed numerical scheme, and the generated results are presented at two time instances in Figures 9(b) and 9(c).

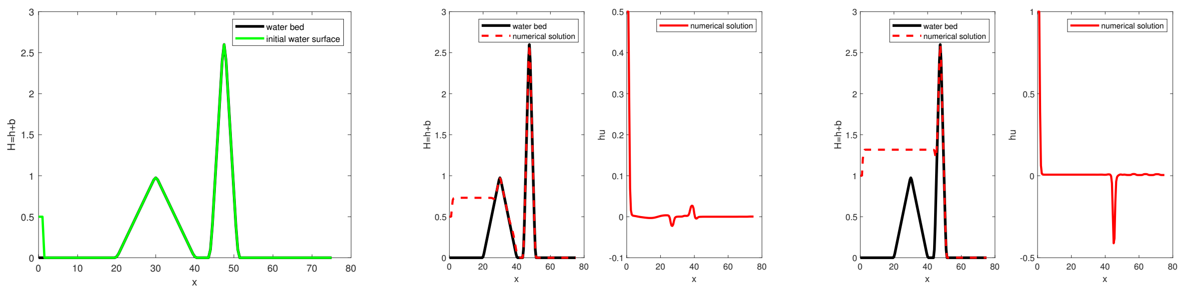

(a) Initial water surface profile $H = h + b$ at $t = 0$. **(b)** Water surface profile $H = h + b$ at $t = 300$. **(c)** Water surface profile $H = h + b$ at $t = 540$.

Figure 9. Problem 7: Flooding on a channel with two mounds. The left panel shows the initial water surface profile $H = h + b$ at $t = 0$, while the middle and right panels show the computed water surface profiles at $t = 300$ and $t = 540$, respectively.

The numerical profiles are in good agreement with the corresponding two-dimensional results reported in the reference, indicating that the method captures the essential flooding dynamics accurately.

3.8. Laboratory dam break over a triangular hump

This test case, adapted from the laboratory dam-break experiment over a triangular hump reported in [17], is used to assess the performance of the proposed scheme in a realistic unsteady setting involving wet–dry transitions and wave reflections. The setup consists of a horizontal channel of length 38 m, with the dam located 15.5 m from the upstream boundary. Initially, a still-water reservoir with a depth of 0.75 m occupies the upstream region. A symmetric triangular hump with a height of 0.4 m is positioned 13 m downstream of the dam, with both slopes extending over 3 m.

In [17], a constant Manning coefficient $n = 0.0125$ is used throughout the domain to account for bottom friction. In contrast, the present simulations are performed using a frictionless shallow water model by setting the Manning coefficient to zero. As a result, some discrepancies with the experimental measurements are expected, particularly during later stages of the flow evolution, where friction effects become more significant. This explains the slight differences in the water depth profiles observed in Figures 10(b)–10(d). The upstream and downstream boundaries are treated as a solid wall and an open outlet, respectively. The simulation is carried out up to $t = 90$ s on a uniform grid with a spacing of 5 cm.

At $t = 0$, the dam is instantaneously removed, allowing the upstream reservoir to flow into the downstream region. After about 3 s, the wet–dry front reaches the triangular hump and begins to pass over it. By approximately $t = 5$ s, the flow has propagated further downstream across the floodplain. During this phase, the interaction between the flow and the bed topography produces a shock wave traveling upstream, while a rarefaction wave propagates downstream, leading to a reduction in the water depth over the hump. At approximately $t = 24$ s, the upstream-moving shock reflects at the wall, generating a secondary shock that propagates downstream. By this stage, the crest and downstream face of the hump have become dry, and drying progresses further upstream until the reflected wave encounters the obstacle again. The incoming wave subsequently drives water back over the hump, re-submerging it and producing an additional upstream-propagating wave. The initial configuration is displayed in Figure 10 (a), while the time evolution of the water depth at gauges $g1$, $g3$, and $g6$, located at 2 m, 8 m, and 13 m, respectively, is shown in Figures 10(b)–10(d).

Figure 10(a) shows the initial water level of the numerical solution $\mathbf{u}_0$ in solid green. Figures 10(b)–10(d) display the time histories of the water depth at gauges $g1$, $g3$, and $g6$, respectively, where the experimental measurements are shown by the solid blue curves and the numerical results of the proposed scheme are shown by the dashed red curves. The proposed scheme reproduces the main stages of the experimental evolution well, including inundation, drying, and wave reflection over the hump. The differences from the experimental measurements remain consistent with the fact that bottom friction is neglected in the present simulations.

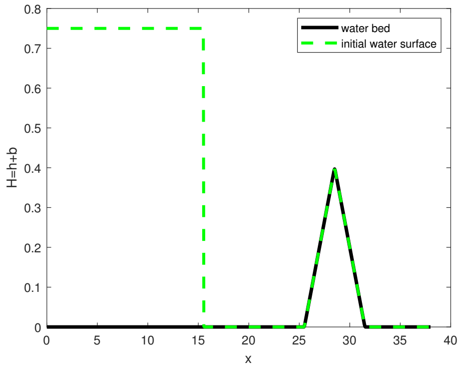

(a) Initial water surface profile $H = h+b$ at $t = 0$.

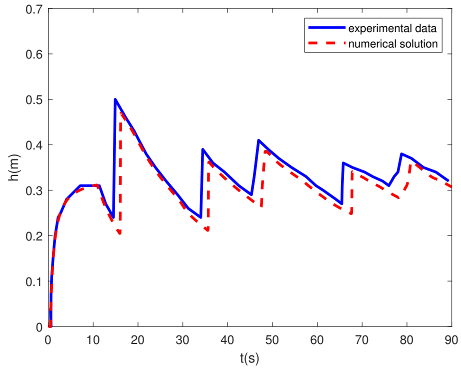

(b) Time history of water depth h at gauge $g1$.

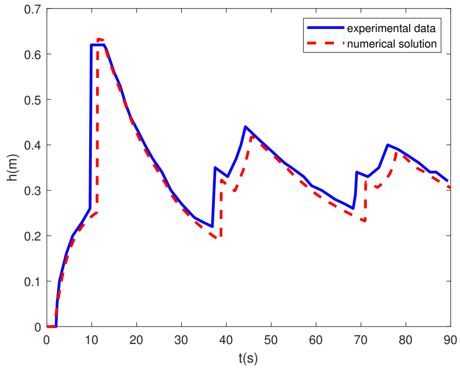

(c) Time history of water depth h at gauge $g3$.

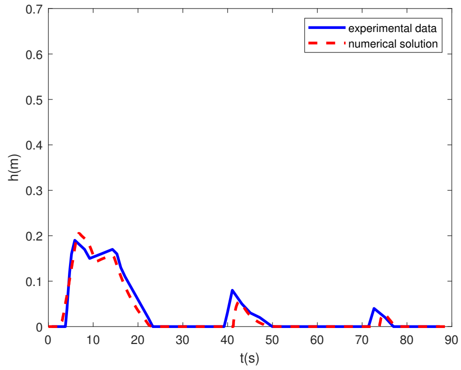

(d) Time history of water depth h at gauge $g6$.

Figure 10. Problem 8: Laboratory dam-break test over a triangular hump. The top left panel shows the initial water surface profile $H = h + b$ at $t = 0$. The remaining panels display the time histories of the water depth h at gauges $g1$, $g3$, and $g6$, respectively. In the gauge plots, the experimental measurements are represented by the solid blue curves, while the numerical results obtained using the proposed scheme are shown by the dashed red curves.

To provide a quantitative comparison with the experimental measurements, we computed the root mean square error (RMSE) and the maximum absolute error between the numerical and experimental water depth time histories at gauges $g1$, $g3$, and $g6$. The numerical gauge values were interpolated at the experimental sampling times before computing the error metrics.

Table 4 shows good overall agreement between the numerical and experimental measurements at all three gauges. The smallest discrepancies are observed at gauge $g6$, where both the RMSE and maximum error remain relatively small. Slightly larger discrepancies are observed at gauges $g1$ and $g3$, particularly near the wave front and during peak wave propagation, where stronger transient effects and steep gradients are present.

Table 4. Problem 8 (Laboratory dam-break over a triangular hump): Quantitative comparison between numerical and experimental water-depth measurements at gauges $g1$, $g3$, and $g6$, using the RMSE and maximum absolute error.

Gauge	RMSE (m)	Max. error (m)
$g1$	5.6678e-02	2.7955e-01
$g3$	6.3094e-02	3.7812e-01
$g6$	2.2094e-02	8.0000e-02

In addition, the discrepancies become more noticeable during later stages of the flow's evolution, where accumulated modeling differences become more significant. In particular, since the present numerical model neglects bottom friction, whereas friction effects are present in the experimental setup, part of these discrepancies can be attributed to the absence of friction, which affects both the wave's amplitude and propagation speed.

Therefore, these discrepancies should be interpreted as quantitative indicators of agreement with the experimental measurements rather than as pure numerical discretization errors. Overall, the results confirm that the proposed scheme accurately captures the main features of the dam-break dynamics and reproduces the experimental gauge measurements with good accuracy.

4. Preliminary two-dimensional numerical examples

The theoretical developments of this paper are restricted to the one-dimensional SWE. The numerical examples presented in this section are included solely to illustrate that the proposed reconstruction can be incorporated into an existing two-dimensional central finite-volume framework.

These examples should therefore be regarded as preliminary numerical illustrations of the potential applicability of the proposed approach in higher dimensions, rather than as a complete two-dimensional formulation. In particular, a full two-dimensional extension, including the corresponding limiter, source term discretization, and wet–dry treatment, is not developed in the present work.

4.1. Flow on a V-shaped topography

For our first test case, we extend the one-dimensional V-shaped problem introduced in [16] to a two-dimensional framework, where a localized water mass is released over a V-shaped bottom topography. This example assesses the ability of the method to capture the propagation of a wetting front over sloping terrain. The bottom topography is defined as $b(x, y) = |x - 1|/\sqrt{3}$.

The initial water height is set as a compact parabolic profile, while the velocity is initially zero

$$h(x, y, 0) = \max\left(0, -1.5\,(x - 0.3)\,(x - 0.7)\right),$$
$$u(x, y, 0) = 0.$$

The computational domain $[0, 2] \times [0, 0.25]$ is discretized using 400×25 cells, and the numerical solution is reported at time $t = 0.7$. Free boundary conditions are imposed and implemented using linear extrapolation in the ghost cells.

Figure 11 (left) illustrates the initial location of the water mass together with the water level profile at the final time (right) over the two-dimensional V-shaped domain. The solid red curve represents the water level profile of the corresponding one-dimensional problem from [16], computed using the solver developed in this paper. Both the one- and two-dimensional results are in excellent agreement with the solution reported in [16], providing preliminary numerical evidence of the applicability of the proposed approach to wet–dry problems in two dimensions. The numerical solutions reproduce the expected evolution of the water mass over the bottom topography while preserving the non-negativity of the water height.

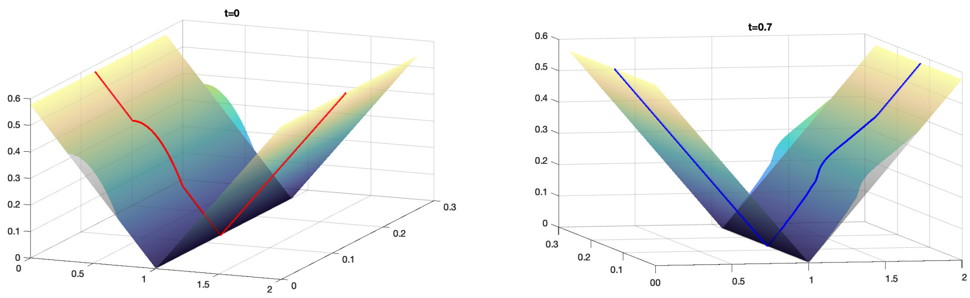

(a) Initial water surface profile $H = h + b$ at $t = 0$. **(b)** Water surface profile $H = h + b$ at $t = 0.7$.

Figure 11. Problem 9: Flow on a V-shaped topography. The left panel shows the initial water surface profile $H = h + b$ at $t = 0$. The right panel shows the water surface profile at $t = 0.7$, including the one-dimensional result (solid red) and the corresponding two-dimensional solution.

4.2. Two symmetric dam breaks

For our last test case, we consider a symmetric dam-break problem over a triangular bottom topography. This configuration produces two waves traveling toward each other across an initially dry central region, making it a suitable test for wave interactions under wetting and drying conditions. The computational domain $[-2, 2]\times[-0.3, 0.3]$ is discretized using 100×40 cells. Reflective boundary conditions are imposed at the left and right boundaries.

The bottom profile is given by

$$b(x, y) = \begin{cases} 1, & x < -1, \\ 2 + x, & -1 \le x \le 0, \\ 2 - x, & 0 \le x \le 1, \\ 1, & x > 1. \end{cases}$$

The initial water height consists of two opposing still-water reservoirs separated by a dry region and is defined as

$$h(x, y, 0) = \begin{cases} 2, & x < -1, \\ 0, & -1 \le x \le 1, \\ 2, & x > 1. \end{cases}$$

with zero initial velocity, $u(x, y, 0) = 0$.

The numerical solution is computed using a preliminary two-dimensional implementation of the proposed approach at different time instances, and the resulting profiles are presented in Figure 12. The figure shows the initial water distribution (left), together with the water elevation profiles at times $t = 0.15$ and $t = 0.49$. The solid red curve denotes the solution of the corresponding one-dimensional problem, which reproduces the expected spreading of the initial water mass over the bottom topography while preserving a non-negative water depth.

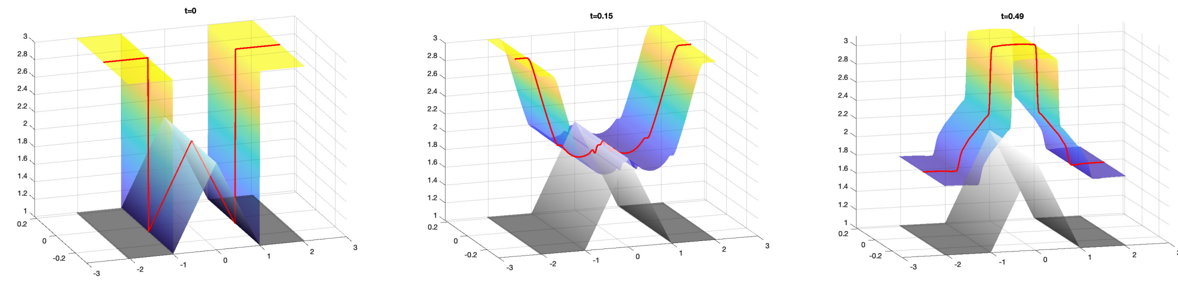

(a) Initial water surface profile $H = h + b$ at $t = 0$. **(b)** Water surface profile $H = h + b$ at $t = 0.15$. **(c)** Water surface profile $H = h + b$ at $t = 0.49$.

Figure 12. Problem 10: Two symmetric dam breaks. The left panel shows the initial water surface profile $H = h + b$ at $t = 0$. The middle and right panels show the water surface profiles at $t = 0.15$ and $t = 0.49$, respectively. The solid red curve denotes the corresponding one-dimensional solution.

5. Conclusions

In this work, we presented a robust central finite-volume method for SWE with wetting and drying that is formally second-order accurate in smooth regimes. The method combines surface gradient reconstruction with an IRP limiter in a consistent framework that ensures both exact well-balancing and the preservation of physically admissible states.

A central feature of the proposed approach is the compatible interaction between the well-balanced reconstruction and the nonlinear limiter. In fully wet regions, explicit cutoff criteria identify when the limiter remains inactive, allowing the scheme to recover the original well-balanced formulation and preserve steady states up to machine precision. The main novelty of this work lies in the treatment of lake-at-rest configurations involving wet–dry interfaces. Through a dedicated wet–dry reconstruction and local balance-law discretization near the interface, the scheme preserves the C-property while maintaining non-negative water heights and exactly preserving dry states.

Numerical experiments provide extensive validation of the proposed method and demonstrate second-order numerical convergence of the water height in smooth benchmark problems, together with robustness for challenging wet–dry configurations involving discontinuous topographies, wet–dry transitions, and dam-break flows.

The proposed scheme provides a reliable and unified Riemann-solver-free framework for simulating shallow water flows with complex geometries and wetting–drying dynamics.

Author contributions

Elissa Malaeb: Methodology, coding and visualization, validation, writing and editing; Toni Sayah: Coordination, supervision, validation, writing–review and editing; Rony Touma: Conceptualization, methodology, validation, supervision, writing–review and editing. All authors have read and approved the final version of the manuscript for publication.

Use of Generative-AI tools declaration

The authors declare they have not used Artificial Intelligence (AI) tools in the creation of this article.

Conflict of interest

The authors declare no conflicts of interest.

References

1. H. Nessyahu, E. Tadmor, Non-oscillatory central differencing for hyperbolic conservation laws, *J. Comput. Phys.*, **87** (1990), 408–463. http://doi.org/10.1016/0021-9991(90)90260-8
2. G. S. Jiang, D. Levy, C. T. Lin, S. Osher, E. Tadmor, High-resolution non-oscillatory central schemes with non-staggered grids for hyperbolic conservation laws, *SIAM J. Numer. Anal.*, **35** (1998), 2147–2168 https://doi.org/10.1137/S0036142997317560
3. J. G. Zhou, D. M. Causon, C. G. Mingham, D. M. Ingram, The surface gradient method for the treatment of source terms in the shallow-water equations, *J. Comput. Phys.*, **168** (2001), 1–25. https://doi.org/10.1006/jcph.2000.6670
4. R. Touma, S. Khankan, Well-balanced unstaggered central schemes for one and two-dimensional shallow water equation systems, *Appl. Math. Comput.*, **218** (2012), 5948–5960. https://doi.org/10.1016/j.amc.2011.11.059
5. A. Kurganov, Finite-volume schemes for shallow-water equations, *Acta Numer.* **27** (2018), 289–351. https://doi.org/10.1017/S0962492918000028
6. A. Kurganov, R. X. Xin, New low-dissipation central-upwind schemes, *J. Sci. Comput.*, **96** (2023), 56. https://doi.org/10.1007/s10915-023-02281-8
7. M. J. Castro, C. Pares, G. Puppo, G. Russo, Central schemes for nonconservative hyperbolic systems, *SIAM J. Sci. Comput.*, **34** (2012), B523–B558. https://doi.org/10.1137/110828873
8. A. Kurganov, G. Petrova, A second-order well-balanced positivity-preserving central-upwind scheme for the Saint–Venant system, *Commun. Math. Sci.*, **5** (2007), 133–160. https://doi.org/10.4310/CMS.2007.v5.n1.a6
9. A. Bollermann, G. X. Chen, A. Kurganov, S. Noëlle, A well-balanced reconstruction of wet/dry fronts for the shallow water equations, *J. Sci. Comput.*, **56** (2013), 267–290. https://doi.org/10.1007/s10915-012-9677-5

10. Y. L. Xing, C. W. Shu, High-order finite volume WENO schemes for the shallow water equations with dry states, *Adv. Water Resour.*, **34** (2011), 1026–1038. https://doi.org/10.1016/j.advwatres.2011.05.008

11. Y. Liu, J. F. Lu, Q. Tao, Y. H. Xia, An oscillation-free discontinuous Galerkin method for shallow water equations, *J. Sci. Comput.*, **92** (2022), 109. https://doi.org/10.1007/s10915-022-01893-w

12. W. Barsukow, J. P. Berberich, A well-balanced active flux method for the shallow water equations with wetting and drying, *Commun. Appl. Math. Comput.*, **6** (2024), 2385–2430. https://doi.org/10.1007/s42967-022-00241-x

13. R. Touma, F. Kanbar, Well-balanced central schemes for two-dimensional systems of shallow water equations with wet and dry states, *Appl. Math. Model.*, **62** (2018), 728–750. https://doi.org/10.1016/j.apm.2018.06.032

14. R. Touma, Well-balanced central schemes for systems of shallow water equations with wet and dry states, *Appl. Math. Model.*, **40** (2016), 2929–2945. https://doi.org/10.1016/j.apm.2015.09.073

15. R. F. Yan, W. Tong, G. X. Chen, A mass conservative, well balanced and positivity-preserving central scheme for shallow water equations, *Appl. Math. Comput.*, **443** (2023), 127778. https://doi.org/10.1016/j.amc.2022.127778

16. A. Chertock, S. Cui, A. Kurganov, T. Wu, Well-balanced positivity-preserving central-upwind scheme for the shallow water system with friction terms, *Int. J. Numer. Meth. Fl.*, **78** (2015), 355–383. https://doi.org/10.1002/fld.4023

17. Q. H. Liang, F. Marche, Numerical resolution of well-balanced shallow water equations with complex source terms, *Adv. Water Resour.*, **32** (2009), 873–884. https://doi.org/10.1016/j.advwatres.2009.02.010

18. R. Abgrall, Y. L. Liu, A new approach for designing well-balanced schemes for the shallow water equations: A combination of conservative and primitive formulations, *SIAM J. Sci. Comput.*, **46** (2024), A3375–A3400. https://doi.org/10.1137/23M1624610

19. A. Chertock, A. Kurganov, X. Liu, Y. L. Liu, T. Wu, Well-balancing via flux globalization: Applications to shallow water equations with wet/dry fronts, *J. Sci. Comput.*, **90** (2022), 9. https://doi.org/10.1007/s10915-021-01680-z

20. R. T. Alqahtani, J. C. Ntonga, E. Ngondiep, Stability analysis and convergence rate of a two-step predictor-corrector approach for shallow water equations with source terms, *AIMS Math.* **8** (2023), 9265–9289. https://doi.org/10.3934/math.2023465

21. K. Farooq, E. Hussain, H. A. Abujabal, F. S. Alshammari, Propagation of non-linear dispersive waves in shallow water and acoustic media in the framework of integrable Schwarz–Korteweg–de Vries equation, *AIMS Math.* **10** (2025), 17543–17566. https://doi.org/10.3934/math.2025784

22. D. Y. Le Roux, A. Staniforth, C. A. Lin, Finite elements for shallow-water equation ocean models, *Mon. Weather Rev.*, **126** (1998), 1931–1951.

23. R. Comblen, S. Legrand, E. Deleersnijder, V. Legat, A finite element method for solving the shallow water equations on the sphere, *Ocean Model.*, **28** (2009), 12–23. https://doi.org/10.1016/j.ocemod.2008.05.004

24. F. Nudo, Two one-parameter families of nonconforming enrichments of the Crouzeix–Raviart finite element, *Appl. Numer. Math.*, **203** (2024), 160–172. https://doi.org/10.1016/j.apnum.2024.05.023

25. F. Dell'Accio, A. Guessab, F. Nudo, New quadratic and cubic polynomial enrichments of the Crouzeix–Raviart finite element, *Comput. Math. Appl.*, **170** (2024), 204–212. https://doi.org/10.1016/j.camwa.2024.06.019

26. Y. L. Xing, X. X. Zhang, Positivity-preserving well-balanced discontinuous Galerkin methods for the shallow water equations on unstructured triangular meshes, *J. Sci. Comput.*, **57** (2013), 19–41. https://doi.org/10.1007/s10915-013-9695-y

AIMS Press